



*Supplement of*

## **Dilution impacts on smoke aging: evidence in Biomass Burning Observation Project (BBOP) data**

**Anna L. Hodshire et al.**

*Correspondence to:* Anna L. Hodshire (Anna.Hodshire@colostate.edu)

The copyright of individual parts of the supplement might differ from the article licence.

## Sect. S1. Further details on BBOP instrumentation

The Fast Integrated Mobility Spectrometer (FIMS) characterizes particle sizes based on electrical mobility similar to the operating principle of the scanning mobility particle sizer (SMPS). Because the FIMS measures particles of different sizes simultaneously instead of sequentially as in traditional SMPS, it provides aerosol size distribution with a much higher time resolution at 1 Hz (Wang et al., 2017). The relative humidity of the aerosol sample was reduced to below ~25% using a Nafion dryer before being introduced into the FIMS. Therefore, the measured size distributions represented that of the dry aerosol particles. The particle number concentration integrated from FIMS size distribution typically agrees with the CPC 3010 (Condensation Particle Counter) measurement (Kleinman et al., 2020) within ~ 15% when size distribution suggests that particles smaller than 20 nm contribute negligibly to the total number concentration. Thus, we estimate the uncertainty in the FIMS number concentration to be ~15%. The uncertainty in measured particle size is about 3% (Wang et al., 2017).

The Soot Particle Aerosol Mass Spectrometer (SP-AMS) is thoroughly detailed in Kleinman et al. (2020). Although it was not directly characterized for uncertainties during the BBOP campaign, we estimate uncertainties as follows. The AMS uncertainty is estimated following the methods in [\(Bahreini et al. 2009\)](#) (first equation of their supplemental information), leading to 37% uncertainty for organics. The laser vaporizer adds additional uncertainty up to 20%. Thus summing the uncertainties in quadrature leads to a 42% uncertainty in organics. The Soot Photometer (SP2) had an uncertainty of 20%.

CO measurement uncertainties are detailed in Kleinman et al. (2020): the Off-Axis Integrated Cavity Output Spectroscopy was found to have an accuracy of 1-2%, and the precision at ambient backgrounds of 90 ppb was 0.5 ppbv RMS (using a 1 second averaging).

An SPN1 radiometer (Badosa et al., 2014; Long et al., 2010) measured total shortwave irradiance, with a shaded mask applied following Badosa et al. (2014). The data was corrected for tilt up to 10 degrees of tilt, following Long et al. (2010). For tilt greater than 10 degrees these values are set to "bad". Instrument uncertainties are detailed in [Badosa et al. \(2014\)](#).

The Soot Particle – Aerosol Mass Spectrometer (SP-AMS) operating on the DOE G1 aircraft during BBOP has been described in detail by Collier et al. (2016), Sedlacek et al. (2018), and Kleinman et al. (2020). The SP-AMS sampled PM<sub>1</sub> through a constant pressure inlet operating at a pressure of ~620 Torr (Bahreini et al., 2008). The SP-AMS was equipped with dual vaporizers: (1) standard resistively heated tungsten vaporizer; and (2) 1064 nm intracavity laser vaporizer (Onasch et al., 2012). The standard tungsten vaporizer was operated at a nominal value of 600°C for the full data set. The SP-AMS operating with the laser vaporizer OFF is effectively the same as a standard HR-AMS, measuring non-refractory particulate matter (NR-PM). The SP-AMS operating in dual vaporizer mode, with both the standard tungsten vaporizer and the laser vaporizer ON measures the NR-PM and is additionally sensitive to refractory black carbon (rBC).

Flight data was collected at a rapid rate using “Fast-MS” in V-mode (i.e., mass spectral resolution  $\sim 2000$ ) with 1 second sample time, with negligible particle time-of-flight (PTOF) data (DeCarlo et al., 2006; Lack et al., 2009). The pulsed, orthogonal extraction time-of-flight mass spectrometer (TOF-MS) was operated with a 60  $\mu\text{s}$  pulser period and collected mass spectra from  $m/z$  11 to  $m/z$  955. “Fast-MS” data was collected in open (i.e., sample) mode for 52 seconds and in closed (i.e., background) mode for 8 seconds every minute. The laser vaporizer was operated by either automatically alternated laser ON and OFF each minute or manually sampling with the laser ON or OFF for long periods of time, such as full plume transects. The majority of the data ( $>76\%$ ) was collected in dual vaporizer mode (i.e., laser on).

The SP-AMS was calibrated for NR-PM with ammonium nitrate and for rBC with Regal black 8 independent times during BBOP. The average ionization efficiency (IE) with respect to ammonium nitrate was measured to be  $8.1\text{e-}8$  and the relative ionization efficiency (RIE) of rBC was measured to be 0.28, although the rBC from the SP-AMS was not used in this study.

Collier et al. (2016) determined the SP-AMS laser OFF collection efficiency (CE) to be 0.5 through comparisons with an independent HR-AMS located at the Mount Bachelor Observatory during over-flights. SP-AMS measured NR-PM values collected with the laser ON and OFF were compared for 16 different biomass burning plumes (Sedlacek et al., 2018; Kleinman et al., 2020). In each case, the plume was sampled with the laser ON and with the laser OFF, independently, and the measured plume NR-PM was normalized to CO to account for potential changes in the plume dilution between transects. The average ratio for NR-PM laser ON to laser OFF was 1.52. From these results, the average CE of NR-PM measured with the laser ON to be 0.76 with a standard deviation of 0.07 (Sedlacek et al., 2018; Kleinman et al., 2020). There is substantial evidence in the published literature for the CE of the tungsten vaporizer (Lim et al., 2019) and the laser vaporizer (Willis et al., 2014) to change as a function of chemical composition and rBC coating thickness. Unfortunately for various reasons, instrument comparisons of measurements of  $\text{PM}_1$  mass loading concentrations were very limited during BBOP, such that there does not exist a useful estimate of a changing CE for either SP-AMS vaporizer with changing plume conditions.

The SP-AMS data was analyzed using ToF-AMS Analysis Toolkit 1.61B and ToF-AMS HR Analysis 1.21B in Igor Pro. Gas phase carbon dioxide ( $\text{CO}_2$ ) was directly measured on the G1 aircraft and was used to subtract gas phase contributions to  $\text{CO}_2^+$  ion signal in the SP-AMS. SP-AMS standard NR-PM chemical species (i.e., Org,  $\text{SO}_4$ ,  $\text{NO}_3$ ,  $\text{NH}_4$ , Chl) were calculated using high resolution (HR) fits.  $f_{44}$  and  $f_{60}$  are unit mass resolution (UMR) ratios, whereas O:C ratios were derived using HR fits. Although it was not directly characterized for uncertainties during the BBOP campaign, we estimate uncertainties as follows. The AMS uncertainty is estimated following the methods in (Bahreini et al. 2009) (first equation of their supplemental information), leading to 37% uncertainty for organics. The laser vaporizer adds additional uncertainty up to 20%. Thus summing the uncertainties in quadrature leads to a 42% uncertainty in organics. (The Soot Photometer (SP2) had an uncertainty of 20%.)

We further analyzed the UMRs and the potential for laser ON specific ion signals to interfere with laser OFF NR-PM ion signals with the SP-AMS data. The chemical composition of the measured wildfire plumes during BBOP were > 90% NR-PM organic material (Collier et al., 2016; Kleinman et al., 2020). rBC mass fractions were typically below 2% (Kleinman et al., 2020), though the number fractions were higher (Sedlacek et al., 2018). Despite these low concentrations, the SP-AMS laser ON (relative to laser OFF) was observed to generate  $C_n^+$  ion signals with an identifiable fragmentation pattern for rBC material and the laser ON to OFF NR-PM signal was observed to increase by ~50% on average. Similar results have been published for ambient urban aerosol (e.g., Lee et al. 2015). Recent laboratory work to investigate these issues has eliminated laser alignment issues and indirect heating as potential causes for these observations (Avery et al., 2020). Thus, these observations are likely due to a combination of different collection efficiencies (CEs) and relative ionization efficiencies (RIEs) for the two vaporizers when used in dual vaporizer mode (i.e., laser ON).

The HR ion signals at  $m/z$  44 are dominated by  $CO_2^+$  and  $C_2H_4O^+$  ions (Fig. S31). The ratio of  $C_2H_4O^+/CO_2^+$  increases with plume mass loading (i.e., concentration) and decreases with distance from the fire (Fig. S31), inline with the observations reported here for decreases in oxidation levels as a function of dilution. The HR ion signals at  $m/z$  60 are dominated by  $C_2H_4O_2^+$  and  $C_5^+$  (Fig. S32). HR fitting of  $C_5^+$  indicated that it averaged ~6% of the  $C_2H_4O_2^+$  ion signal, independent of the laser vaporizer state (i.e., ON or OFF). For large  $C_2H_4O_2^+$  ion signals in relatively undiluted biomass burning plumes, this ratio is likely controlled by the errors in fitting a small peak in the wings of a larger peak (Corbin et al., 2014). At lower ion signal levels, the  $C_5^+/C_2H_4O_2^+$  becomes significantly noisier, but the average does not change significantly. Laser ON may slightly increase the average ratio at lower  $C_2H_4O_2^+$  ion signals, which could overestimate  $f_{60}$  for relatively dilute plumes. If this were true, the observed decrease in  $f_{60}$  with plume dilution (i.e., due to fire size and atmospheric age) would be slightly smaller than reported here.

Past research on SP-AMS ion signals from the laser vaporizer and the standard tungsten vaporizer have identified several complicating factors when operating the SP-AMS in dual vaporizer mode. First, organic material coating rBC particles and detected using the laser vaporizer have noted different fragmentation patterns (Onasch et al., 2012) and chemical compositions (Canagaratna et al., 2015) compared with the same organic material detected using the standard tungsten vaporizer. Further, there are reports of SP-AMS laser vaporizer detecting refractory  $CO_2^+$  ions from rBC particles (Corbin et al., 2014). Currently, we have not assessed the potential for refractory  $CO_2^+$  ion signals during BBOP as both the rBC and Org signals are highly correlated in biomass burning plumes, making minor changes to these ratios difficult to ascertain. To address the question of whether the laser vaporizer generated different ion signals from similar organic compounds, we analyzed the laser ON and OFF plume transect pairs that were used for determining laser ON CE values relative to laser OFF.

As shown in Fig. S33, the HR O:C, UMR  $f_{44}$ , and UMR  $f_{60}$  ratios are highly correlated between laser ON and OFF conditions, though differ by apparent factors. Laser ON HR O:C ratios are approximately 4% lower than laser OFF. In large part, this is due to the UMR  $f_{44}$  ratios, which are dominated by  $\text{CO}_2^+$  ions, being 17% lower for laser ON. UMR  $f_{60}$  ratios are 18% higher in laser ON than OFF. These observations are in line with the published results from Canagaratna et al., (2015), which observed that laser vaporizer only HR O:C ratios were ~17% lower than tungsten vaporizer only HR O:C ratios for the same organic material and the HR H:C ratios were ~16% higher. In the case of BBOP, the laser vaporizer signals represented approximately 1/3 of the total organic signal with dual vaporizers. The BBOP measured 4% lower HR O:C ratios are similar in magnitude to 5.6% (i.e.,  $0.33 \times 17\%$ ) expected if the Canagaratna et al. (2015) results applied to BBOP measurements.

The BBOP SP-AMS data used in this manuscript is used to measure trends in OA. O:C,  $f_{44}$ , and  $f_{60}$  with plume dilution, either at different plume ages and/or different concentration percentiles across a biomass plume (i.e., edge vs. center). A question is whether the mixing of laser ON and OFF data here somehow biases the results due to the different absolute values between the two different states. A quick extension of the above plume pair analysis (Fig. S33) includes several “background” measurements made between the plumes (i.e., below 150 ppbv CO) and compared for laser ON vs. OFF to investigate if this ratio changes substantially between plume (i.e., high level) and background (i.e., low level) levels. The laser ON:OFF ratios of measured HR O:C averaged  $0.95 \pm 0.049$  in background and  $0.96 \pm 0.029$  in plume, UMR  $f_{44}$  averaged  $0.89 \pm 0.085$  in background and  $0.85 \pm 0.068$  in plume, and UMR  $f_{60}$  averaged  $1.17 \pm 0.23$  in background and  $1.15 \pm 0.13$  in plume. These results suggest that the observed laser ON/OFF ratios do not change from low to high signal levels, such that the trends observed for laser OFF should hold for laser ON, and vice versa. Further, the laser ON vs. OFF data points are randomly distributed throughout the measurements rather than systematically distributed to near- vs. far-field measurements or core vs. edge measurements. Hence, there should be no systematic bias due to the use of the combined laser ON and OFF data, although this combination of laser-on and -off data may contribute to noise in the observed trends.

## Sect. S2. Heterogeneous chemistry calculations

We test the impact of heterogeneous chemistry on aerosol mass loss within the smoke plume. We performed a simple calculation of reactive uptake of OH molecules with particle-phase organics that resulted in loss of organic products. These calculations include assumed values of particle diameter, OH concentration, OH diffusion coefficient, and OH reactive uptake coefficient. The following parameters are assumed for the calculations:

- OH diffusivity =  $3.5 \times 10^{-5}$  [ $\text{m}^2 \text{s}^{-1}$ ]
- Particle diameter varied from 1 - 1000 [nm]
- Constant OH concentration varied from  $1 \times 10^5$  to  $5 \times 10^7$  [molecules  $\text{cm}^{-3}$ ]
- Reactive uptake coefficients varied from 0.1 to 1 [unitless]

- Molecular weight of organics = 200 [g mol<sup>-1</sup>]
- Density of organics = 1.4 [g cm<sup>-3</sup>]
- Total run time = 3 [hours]

The collision rate of OH with the particle surface was calculated using the condensation equations in Seinfeld and Pandis (2006). As a calculation of the upper bound limit of evaporation due to heterogeneous chemistry, we assume each collision results in removing an organic molecule on the surface of the particle (assumed to be 200 amu), fragmenting and removing the molecule from the particle. The fragmentation products are not assumed to participate in further reaction. Figure S23a shows the resulting final:initial mass ratios after four hours of aging, indicating that for the aerosol sizes containing most of the mass in this study (>100 nm) and under expected OH concentrations (<10<sup>7</sup> cm<sup>-3</sup>), >90% of the aerosol mass remains after 3 hours in all but the cases with a reactive uptake coefficient of 1 and an OH concentration of 10<sup>7</sup> cm<sup>-3</sup>. Note however that (1) the reactive uptake coefficient is likely lower than 1 (Slade and Knopf, 2013), (2) not every reaction will lead to complete evaporation of all products, and (3) OH concentrations are often lower than 10<sup>7</sup> cm<sup>-3</sup> (Juncosa Calahorrano et al., 2020).

Avery, A.M., Williams, L.R., Fortner, E.C., Robinson, W.A., and Onasch, T.B.: Particle detection using the dual-vaporizer configuration of the soot particle Aerosol Mass Spectrometer (SP-AMS). *Aerosol Sci. Technol.*, doi:10.1080/02786826.2020.1844132, 2020.

Bahreini, R.; Dunlea, E. J.; Matthew, B. M.; Simons, C.; Docherty, K. S.; DeCarlo, P. F.; Jimenez, J. L.; Brock, C. A.; Middlebrook, A. M.: Design and Operation of a Pressure-Controlled Inlet for Airborne Sampling with an Aerodynamic Aerosol Lens. *Aerosol Sci. Technol.* 42 (6), 465–471, 2008

Badosa, J., Wood, J., Blanc, P., Long, C. N., Vuilleumier, L., Demengel, D. and Haeffelin, M.: Solar irradiances measured using SPN1 radiometers: uncertainties and clues for development, *Atmospheric Measurement Techniques*, 7, 4267–4283, 2014.

Bahreini, R., Ervens, B., Middlebrook, a. M., Warneke, C., de Gouw, J. a., DeCarlo, P.F., Jimenez, J.L., Brock, C. a., Neuman, J. a., Ryerson, T.B., Stark, H., Atlas, E., Brioude, J., Fried, A., Holloway, J.S., Peischl, J., Richter, D., Walega, J., Weibring, P., Wollny, a. G., and Fehsenfeld, F.C.: Organic aerosol formation in urban and industrial plumes near Houston and Dallas, Texas. *J. Geophys. Res.*, 114:D00F16, 2009.

Canagaratna, M.R., Massoli, P., Browne, E.C., Franklin, J.P., Wilson, K.R., Onasch, T.B., Kirchstetter, T.W., Fortner, E.C., Kolb, C.E., Jayne, J.T., Kroll, J.H., and Worsnop, D.R.: Chemical Compositions of Black Carbon Particle Cores and Coatings via Soot Particle Aerosol Mass Spectrometry with Photoionization and Electron Ionization. *J. Phys. Chem. A*, 119(19):4589–4599, 2015.

Collier, S., Zhou, S., Onasch, T.B., Jaffe, D.A., Kleinman, L., Sedlacek, A.J., Briggs, N.L., Hee, J., Fortner, E., Shilling, J.E., Worsnop, D., Yokelson, R.J., Parworth, C., Ge, X., Xu, J., Butterfield, Z., Chand, D., Dubey, M.K., Pekour, M.S., Springston, S., and Zhang, Q.: Regional Influence of Aerosol Emissions from Wildfires Driven by Combustion Efficiency: Insights from the BBOP Campaign. *Environ. Sci. Technol.*, 50(16):acs.est.6b01617, 2016.

Corbin, J.C., Sierau, B., Gysel, M., Laborde, M., Keller, A., Kim, J., Petzold, A., Onasch, T.B., Lohmann, U., and Mensah, A. A.: Mass spectrometry of refractory black carbon particles from six sources: carbon-cluster and oxygenated ions. *Atmos. Chem. Phys.*, 14(5):2591–2603, 2014.

Corbin, J., Othman, A., D. Allan, J., R. Worsnop, D., D. Haskins, J., Sierau, B., Lohmann, U., and A. Mensah, A. (2015). Peak-fitting and integration imprecision in the Aerodyne aerosol mass spectrometer: effects of mass accuracy on location-constrained fits. *Atmos. Meas. Tech.*, 8(11):4615–4636.

DeCarlo, P.F., Kimmel, J.R., Trimborn, A., Northway, M.J., Jayne, J.T., Aiken, A.C., Gonin, M., Fuhrer, K., Horvath, T., Docherty, K.S., Worsnop, D.R., and Jimenez, J.L.: Field-Deployable, High-Resolution, Time-of-Flight Aerosol Mass Spectrometer. *Anal. Chem.*, 78(24):8281–8289, 2006.

Juncosa Calahorrano, J. F., Lindaas, J., O'Dell, K., Palm, B. B., Peng, Q., Flocke, F., Pollack, I. B., Garofalo, L. A., Farmer, D. K., Pierce, J. R., Collett, J. L., Weinheimer, A., Campos, T., Hornbrook, R. S., Hall, S. R., Ullmann, K., Pothier, M. A., Apel, E. C., Permar, W., Hu, L., Hills, A. J., Montzka, D., Tyndall, G., Thornton, J. A. and Fischer, E. V.: Daytime Oxidized Reactive Nitrogen Partitioning in Western U.S. Wildfire Smoke Plumes, *J. Geophys. Res. Atmos.*, 1–47, doi:10.1029/2020jd033484, 2020.

Kleinman, L. I., Sedlacek, A. J., III, Adachi, K., Buseck, P. R., Collier, S., Dubey, M. K., Hodshire, A. L., Lewis, E., Onasch, T. B., Pierce, J. R., Shilling, J., Springston, S. R., Wang, J., Zhang, Q., Zhou, S. and Yokelson, R. J.: Rapid Evolution of Aerosol Particles and their Optical Properties Downwind of Wildfires in the Western U.S, *Aerosols/Field Measurements/Troposphere/Physics (physical properties and processes)*, doi:10.5194/acp-2020-239, 2020.

Lack, D. A.; Corbett, J. J.; Onasch, T.; Lerner, B.; Massoli, P.; Quinn, P. K.; Bates, T. S.; Covert, D. S.; Coffman, D.; Sierau, B.; Herndon, S.; Allan, J.; Baynard, T.; Lovejoy, E.; Ravishankara, A. R.; Williams, E.: Particulate emissions from commercial shipping: Chemical, physical, and optical properties. *J. Geophys. Res.* 114 (D7), D00F04, 2009.

Lee, A.K.Y., Willis, M.D., Healy, R.M., Onasch, T.B.B., and Abbatt, J.P.D.: Mixing state of carbonaceous aerosol in an urban environment: single particle characterization using the soot particle aerosol mass spectrometer (SP-AMS). *Atmos. Chem. Phys.*, 15(4):1823–1841, 2015.

Lim, C.Y., Hagan, D.H., Coggon, M.M., Koss, A.R., Sekimoto, K., de Gouw, J., Warneke, C., Cappa, C.D., and Kroll, J.H.: Secondary organic aerosol formation from the laboratory oxidation of biomass burning emissions. *Atmos. Chem. Phys.*, 19(19):12797–12809, 2019.

Long, C. N., Bucholtz, A., Jonsson, H., Schmid, B., Vogelmann, A. and Wood, J.: A Method of Correcting for Tilt from Horizontal in Downwelling Shortwave Irradiance Measurements on Moving

Platforms, *The Open Atmospheric Science Journal*, 4(1), 78–87, doi:10.2174/1874282301004010078, 2010.

Onasch, T. B., Trimborn, A., Fortner, E. C., Jayne, J. T., Kok, G. L., Williams, L. R., Davidovits, P. and Worsnop, D. R.: Soot particle aerosol mass spectrometer: Development, validation, and initial application, *Aerosol Sci. Technol.*, 46(7), 804–817, doi:10.1080/02786826.2012.663948, 2012.

Sedlacek III, A.J., Buseck, P.R., Adachi, K., Onasch, T.B., Springston, S.R., and Kleinman, L.: Formation and evolution of tar balls from northwestern US wildfires. *Atmos. Chem. Phys.*, 18(15):11289–11301, 2018.

Seinfeld, J. H. and Pandis, S. N.: *Atmospheric Chemistry and Physics*, 2nd edn., John Wiley and Sons, New York, 2006.

Slade, J. H. and Knopf, D. A.: Heterogeneous OH oxidation of biomass burning organic aerosol surrogate compounds: assessment of volatilisation products and the role of OH concentration on the reactive uptake kinetics, *Phys. Chem. Chem. Phys.*, 15(16), 5898–5915, 2013.

Wang, J., Pikridas, M., Spielman, S. R. and Pinterich, T.: A fast integrated mobility spectrometer for rapid measurement of sub-micrometer aerosol size distribution, Part I: Design and model evaluation, *J. Aerosol Sci.*, 108, 44–55, 2017.

Willis, M.D., Lee, A.K.Y., Onasch, T.B., Fortner, E.C., Williams, L.R., Lambe, A.T., Worsnop, D.R., and Abbatt, J.P.D.: Collection efficiency of the soot-particle aerosol mass spectrometer (SP-AMS) for internally mixed particulate black carbon. *Atmos. Meas. Tech.*, 7(12):4507–4516, 2014.

Table S1. Flight description table.

Flight name, date	Number of sets of pseudo-Lagrangian transects	Fire name	Fuel <sup>1</sup>	
'726a', 07-26-2013	2	Mile Marker 28	grasslands, shrub brush, timber, and timber litter	
'730a', 07-30-2013	1	Colockum Tarps	grass, trees	
'730b', 07-30-2013	2	Colockum Tarps	grass, trees	
'809a', 08-09-2013	1	Colockum Tarps	grass, trees	
'821b', 08-21-2013	1	Government Flats		

<sup>1</sup>When known

<sup>2</sup>Instruments relevant to this study

Table S2. Calculated  $R_{\Delta OA, initial}$  and  $R_{age}$  values for  $\Delta OA/\Delta CO$ ,  $\Delta f_{60}$ ,  $\Delta f_{44}$ ,  $\Delta H/\Delta C$ ,  $\Delta O/\Delta C$ ,  $\Delta N/\Delta CO$ , and  $D_p$  when one flight is left out of the statistical analysis. We include the original R values as the first row for comparison. Red values indicate that the correlation has improved compared to all flights in the statistical analysis (closer to  $\pm 1$ ). Blue values indicate that the correlation has worsened (closer to 0) compared to all flights in the statistical analysis. Black values denote no change in the correlation compared to all flights in the statistical analysis. Note that for flights ‘726a’ and ‘730b’ both sets of Lagrangian transects have been left out.

$\Delta OA/\Delta CO$		
Flight left out, date	Resulting $R_{\Delta OA, initial}$	Resulting $R_{age}$
None	+0.02	+0.03
‘726a’, 07-26-2013	+0.12	0.0
‘730a’, 07-30-2013	+0.02	+0.07
‘730b’, 07-30-2013	+0.17	0.0
‘809a’, 08-09-2013	-0.25	+0.02
‘821b’, 08-21-2013	+0.05	+0.03
$\Delta f_{60}$		
Flight left out, date	Resulting $R_{\Delta OA, initial}$	Resulting $R_{age}$
None	+0.43	-0.26
‘726a’, 07-26-2013	+0.58	-0.38
‘730a’, 07-30-2013	+0.39	-0.37
‘730b’, 07-30-2013	+0.52	-0.19
‘809a’, 08-09-2013	+0.3	-0.21
‘821b’, 08-21-2013	+0.4	-0.26
$\Delta f_{44}$		
Flight left out, date	Resulting $R_{\Delta OA, initial}$	Resulting $R_{age}$
None	-0.55	+0.5
‘726a’, 07-26-2013	-0.63	+0.4

'730a', 07-30-2013	-0.62	+0.54
'730b', 07-30-2013	-0.45	+0.46
'809a', 08-09-2013	-0.54	+0.54
'821b', 08-21-2013	-0.42	+0.57
<b><math>\Delta H/\Delta CO</math></b>		
Flight left out, date	Resulting $R_{\Delta OA, initial}$	Resulting $R_{age}$
None	-0.04	-0.06
'726a', 07-26-2013	-0.04	-0.12
'730a', 07-30-2013	-0.13	-0.2
'730b', 07-30-2013	0.0	-0.16
'809a', 08-09-2013	0.02	-0.01
'821b', 08-21-2013	-0.01	-0.05
<b><math>\Delta O/\Delta CO</math></b>		
Flight left out, date	Resulting $R_{\Delta OA, initial}$	Resulting $R_{age}$
None	-0.45	+0.56
'726a', 07-26-2013	-0.54	+0.46
'730a', 07-30-2013	-0.52	+0.55
'730b', 07-30-2013	-0.21	+0.54
'809a', 08-09-2013	-0.5	+0.61
'821b', 08-21-2013	-0.32	+0.63
<b><math>\Delta N/\Delta CO</math></b>		
Flight left out, date	Resulting $R_{\Delta OA, initial}$	Resulting $R_{age}$
None	-0.03	-0.27
'726a', 07-26-2013	-0.03	-0.13
'730a', 07-30-2013	-0.03	-0.3

'730b', 07-30-2013	-0.21	-0.43
'809a', 08-09-2013	-0.07	-0.2
'821b', 08-21-2013	0.0	-0.37
$\overline{D}_p$		
Flight left out, date	Resulting $R_{\Delta OA, \text{initial}}$	Resulting $R_{\text{age}}$
None	-0.15	+0.53
'726a', 07-26-2013	-0.18	+0.43
'730a', 07-30-2013	-0.17	+0.57
'730b', 07-30-2013	+0.19	+0.63
'809a', 08-09-2013	-0.28	+0.52
'821b', 08-21-2013	-0.18	+0.52

Table S3. Fit coefficients  $a$ ,  $b$ , and  $c$  for the fits shown in Fig. 3 , equation 4. The units of  $a$  are (metric), but note that the units of  $\Delta O A_{\text{initial}}$  must be  $\mu\text{g m}^{-3}$ ; the units of  $b$  are (metric)/hr, and the units of  $c$  are (metric), where (metric) = the units of  $\Delta f_{60}$ ,  $\Delta f_{44}$ ,  $\Delta O/\Delta C$ , or  $\overline{D}_p$ , respectively.

Metric	$a$	$b$	$c$
$\Delta f_{60}$	2.8e-03	-6.4e-04	4.7e-03
$\Delta f_{44}$	-1.1e-02	5.8e-03	4.4e-02
$\Delta O/\Delta C$	-3.6e-02	2.6e-02	0.24
$\overline{D}_p$	-1.5	10	150

Table S4. Fit coefficients  $a$ ,  $b$ , and  $c$  for the fits shown in Fig. S28 , equation 5. The units of  $a$  are (metric); the units of  $b$  are (metric)/hr, and the units of  $c$  are (metric), where (metric) = the units of  $\Delta f_{60}$ ,  $\Delta f_{44}$ ,  $\Delta O/\Delta C$ , or  $\overline{D}_p$ , respectively.

Metric	$a$	$b$	$c$
$\Delta f_{60}$	0.14	-6.6e-02	-5.3
$\Delta f_{44}$	-0.14	0.11	-2.9
$\Delta O/\Delta C$	-7.3e-02	6.1e-02	-1.3
$\overline{D}_p$	-6.3e-03	4.0e-02	5.1

Table S5. Fit coefficients  $a$ ,  $b$ , and  $c$  for the fits shown in Fig. S29, equation 4 (but with  $\Delta N_{\text{initial}}$  in place of  $\Delta O A_{\text{initial}}$ ). The units of  $a$  are (metric); the units of  $b$  are (metric)/hr, and the units of  $c$  are (metric), where (metric) = the units of  $\Delta f_{60}$ ,  $\Delta f_{44}$ ,  $\Delta O/\Delta C$ , or  $\overline{D}_p$ , respectively.

Metric	$a$	$b$	$c$
$\Delta f_{60}$	2.0e-03	-5.4e-04	-1.5e-03
$\Delta f_{44}$	-1.1e-02	5.3e-03	8.4e-02
$\Delta O/\Delta C$	-4.1e-02	2.4e-02	0.4
$\overline{D}_p$	-3.5	10	160

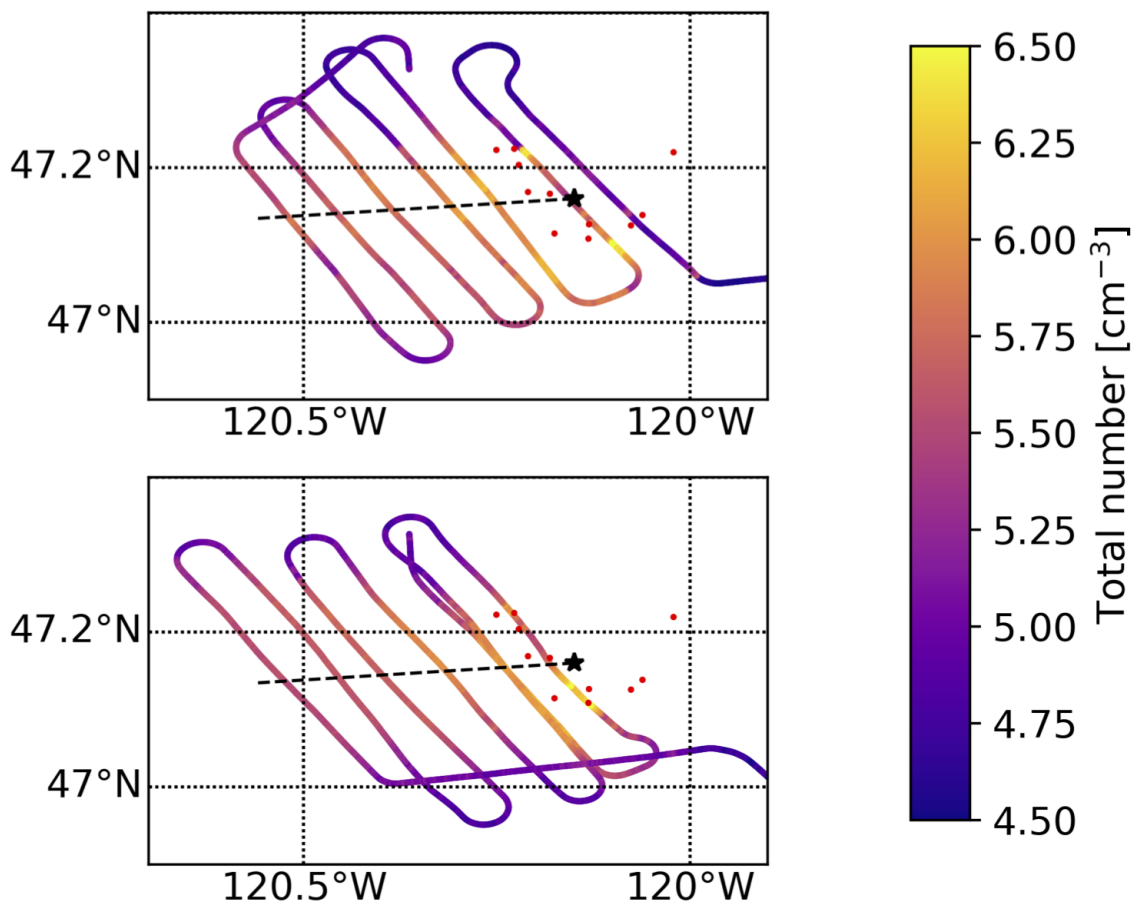


Figure S1. The flight path for flight '730b', colored by the FIMS total number concentration. The red dots are MODIS fire/thermal anomalies. The black star indicates the approximate center of the fire and the black dashed line indicates the approximate centerline of the plume, estimated by the number concentration.

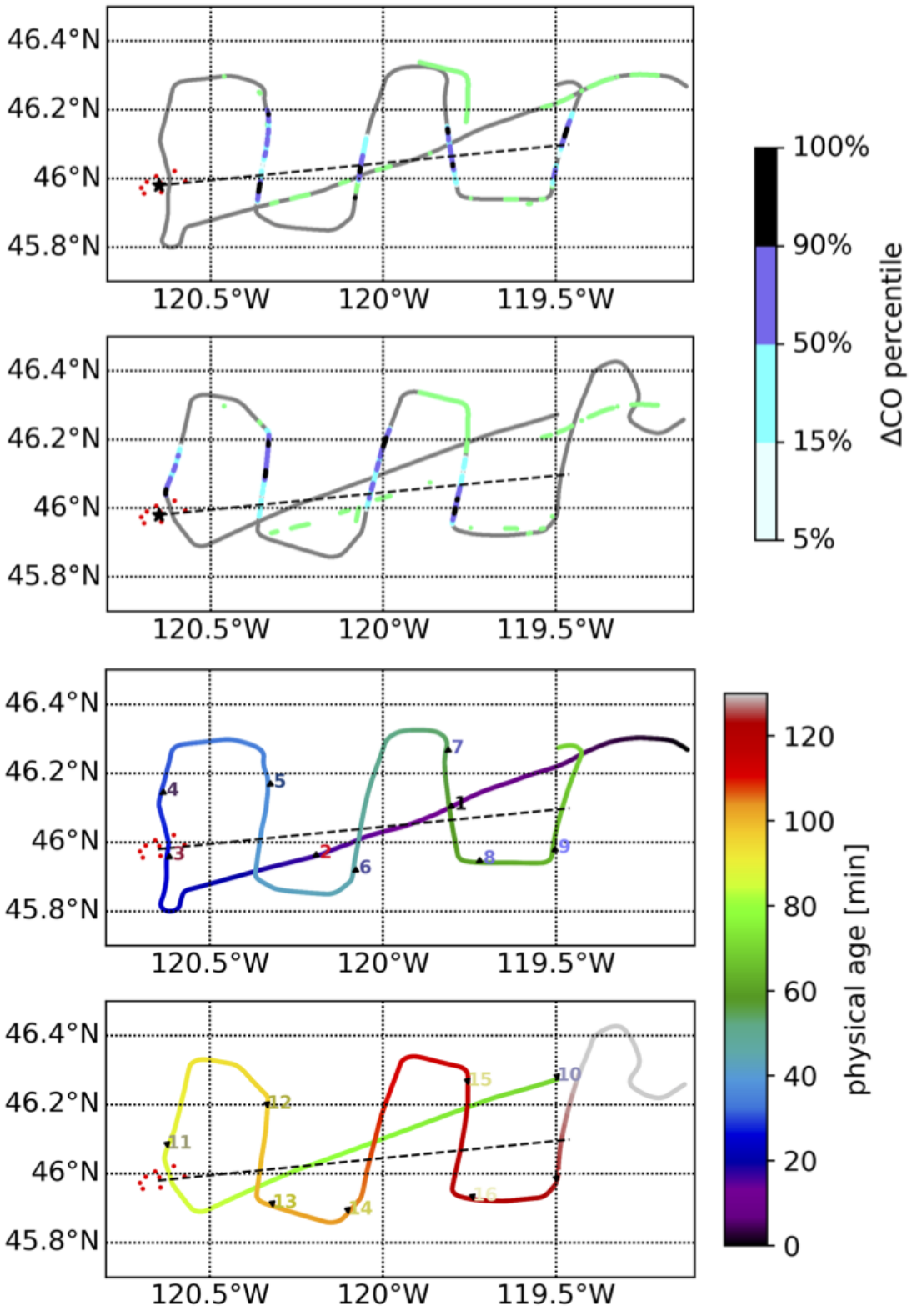


Figure S2. The flight path for '726a'. Top two panels: the legs used in this study are colored by each  $\Delta\text{CO}$  percentile bin used in the main text analyses. The green traces indicate the locations of the lowest 10% of CO, used to compute averaged backgrounds for this flight. Bottom two panels: the flight track colored by time since take-off in minutes. The numbers indicate the leg numbers as identified in the BBOP database. There were two complete flight paths for this day. The red dots are MODIS fire/thermal anomalies. The black star indicates the approximate center of the fire and the black dashed line indicates the approximate centerline of the plume, estimated by the number concentration.

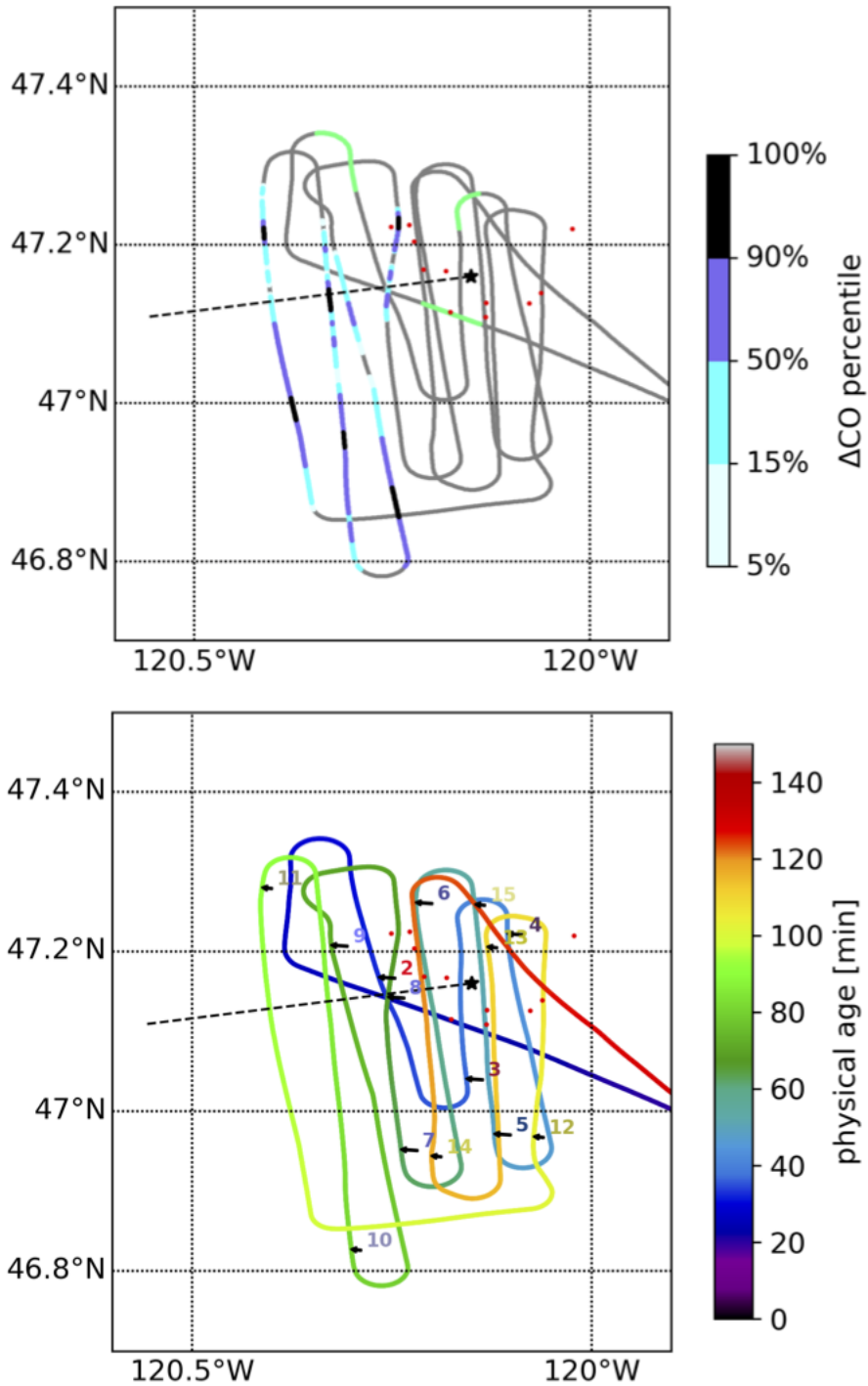


Figure S3. The flight path for ‘730a’. Top panel: the legs used in this study are colored by each  $\Delta\text{CO}$  percentile bin used in the main text analyses. The green traces indicate the locations of the lowest 10% of CO, used to compute averaged backgrounds for this flight. Bottom panel: the flight track colored by time since take-off in minutes. The numbers indicate the leg numbers as

identified in the BBOP database. The red dots are MODIS fire/thermal anomalies. The black star indicates the approximate center of the fire and the black dashed line indicates the approximate centerline of the plume, estimated by the number concentration.

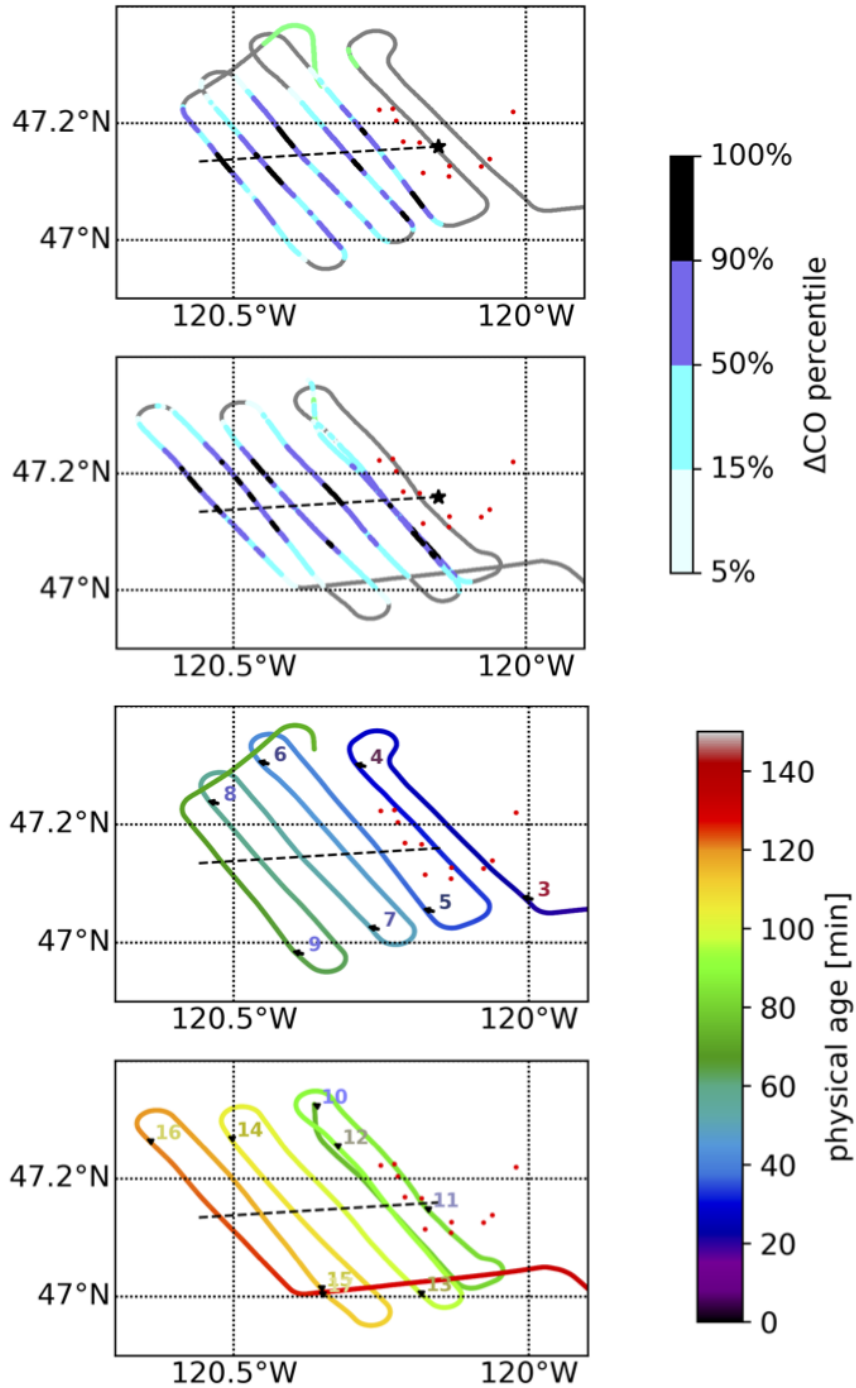


Figure S4. The flight path for '730b'. Top two panels: the legs used in this study are colored by each  $\Delta\text{CO}$  percentile bin used in the main text analyses. The green traces indicate the locations of the lowest 10% of CO, used to compute averaged backgrounds for this flight. Bottom two panels: the flight track colored by time since take-off in minutes. The numbers indicate the leg numbers as identified in the BBOP database. There were two complete flight paths for this flight. The red dots are MODIS fire/thermal anomalies. The black star indicates the approximate center

of the fire and the black dashed line indicates the approximate centerline of the plume, estimated by the number concentration.

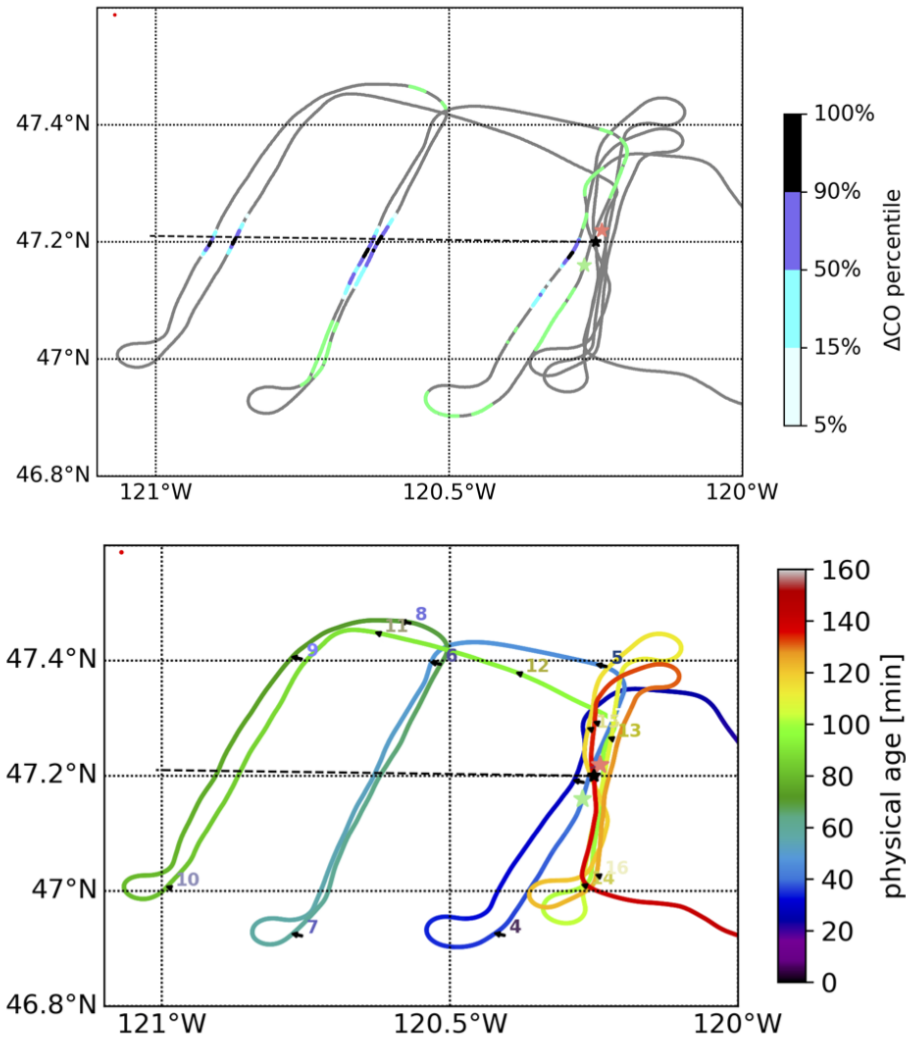


Figure S5. The flight path for ‘809a’. Top panel: the legs used in this study are colored by each  $\Delta\text{CO}$  percentile bin used in the main text analyses. The green traces indicate the locations of the lowest 10% of CO, used to compute averaged backgrounds for this flight. Bottom panel: the flight track colored by time since take-off in minutes. The numbers indicate the leg numbers as identified in the BBOP database. The Worldview image for this day had clouds over the fire location at the time of the satellite passover. Thus we estimate a fire center using Worldview and MODIS images for this region on the previous day (8-08-2013) (light green star) and the following day (8-10-2013) (salmon-colored star). The black star indicates our estimated center of the fire on 8-09-2013 and the black dashed line indicates the approximate centerline of the plume, estimated by the number concentration.

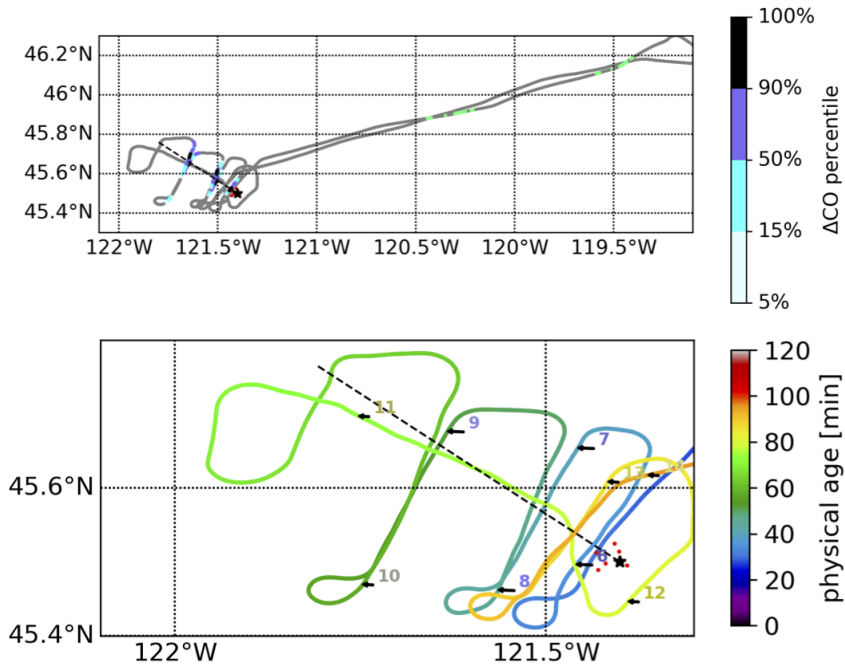


Figure S6. The flight path for '821b'. Top panel: the legs used in this study are colored by each  $\Delta\text{CO}$  percentile bin used in the main text analyses. The green traces indicate the locations of the lowest 10% of CO, used to compute averaged backgrounds for this flight. Bottom panel: the flight track colored by time since take-off in minutes. The numbers indicate the leg numbers as identified in the BBOP database. The red dots are MODIS fire/thermal anomalies. The black star indicates the approximate center of the fire and the black dashed line indicates the approximate centerline of the plume, estimated by the number concentration.

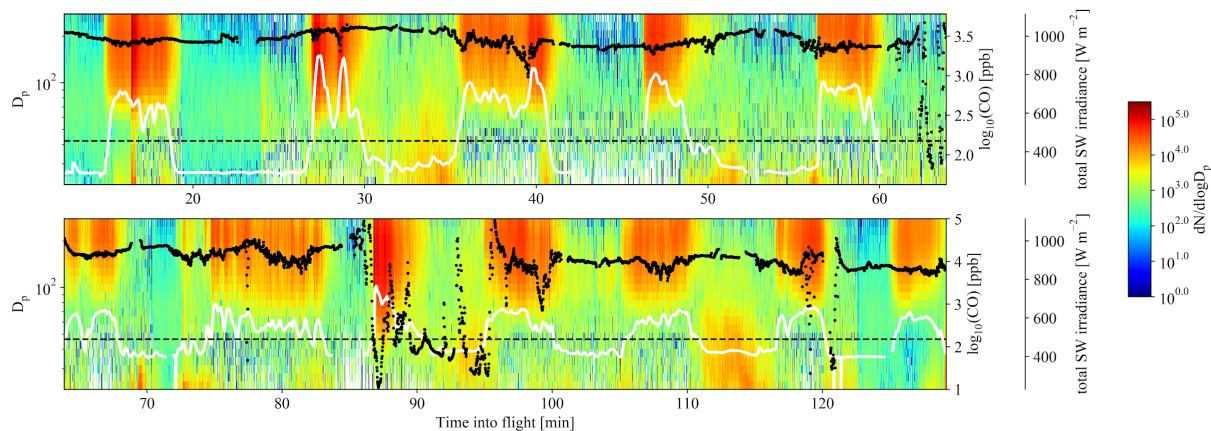


Figure S7. Number size distribution data,  $dN/d\log D_p$ , from the FIMS; CO (white solid line); and total short wave (SW) irradiance (black dots) data for the '726a' flight. The bottom panel is a continuation in time from the top panel. The dotted dashed line indicates CO=150 ppb, our cutoff for in-plume/out-of-plume. The second set of Lagrangian transects for this flight start at the plume at approximately 86 minutes into the flight.

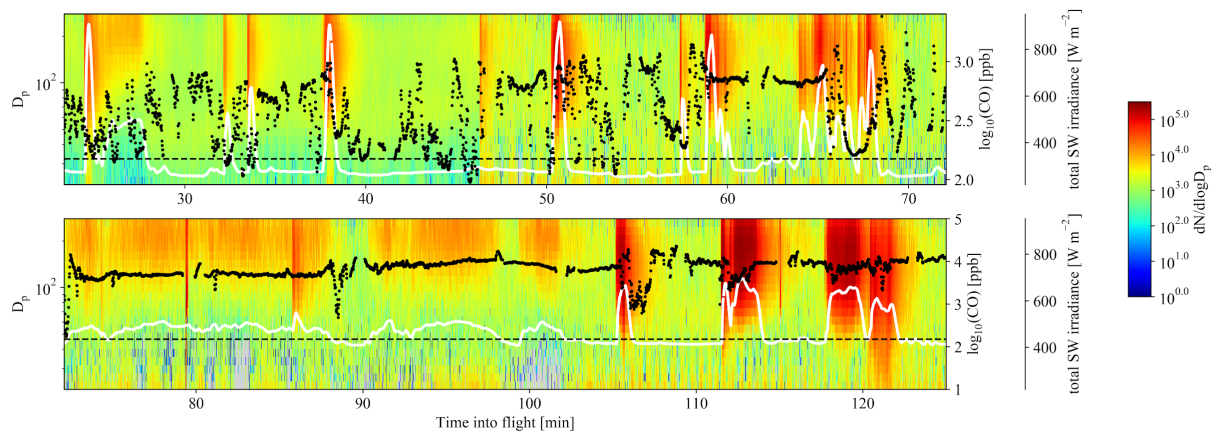


Figure S8. Number size distribution data,  $dN/d\log D_p$ , from the FIMS; CO (white solid line); and total short wave (SW) irradiance (black dots) data for the '730a' flight. The bottom panel is a continuation in time from the top panel. The dotted dashed line indicates CO=150 ppb, our cutoff for in-plume/out-of-plume.

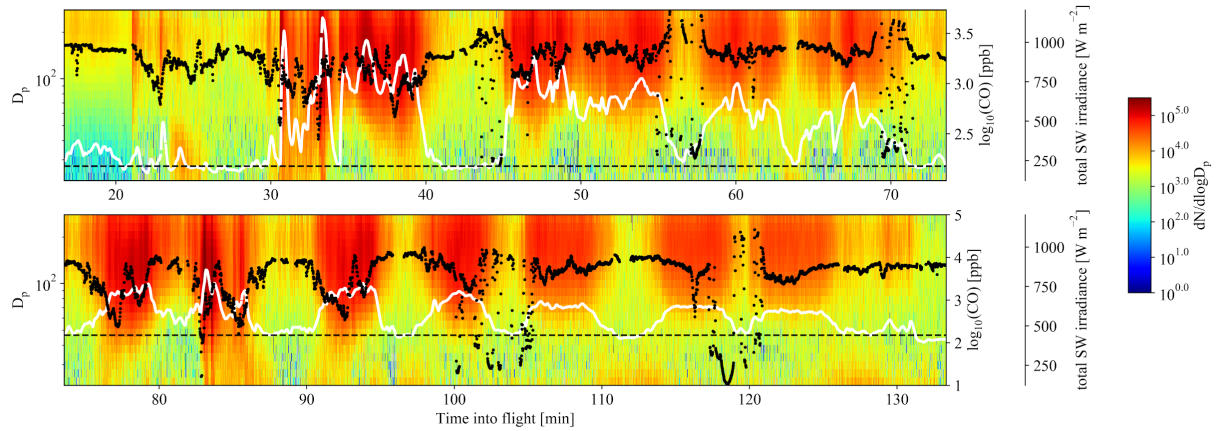


Figure S9. Number size distribution data,  $dN/d\log D_p$ , from the FIMS; CO (white solid line); and total short wave (SW) irradiance (black dots) data for the '730b' flight. The bottom panel is a continuation in time from the top panel. The dotted dashed line indicates CO=150 ppb, our cutoff for in-plume/out-of-plume. For this figure, the top panel contains all of the first Lagrangian set of flight transects, and the bottom panel contains all of the second Lagrangian set of flight transects.

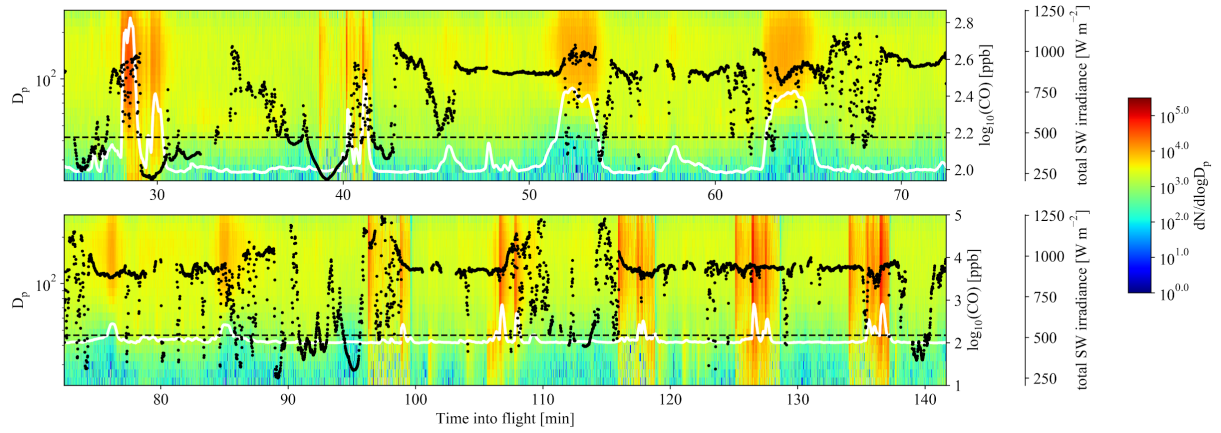


Figure S10. Number size distribution data,  $dN/d\log D_p$ , from the FIMS; CO (white solid line); and total short wave (SW) irradiance (black dots) data for the '809a' flight. The bottom panel is a continuation in time from the top panel. The dotted dashed line indicates CO=150 ppb, our cutoff for in-plume/out-of-plume.

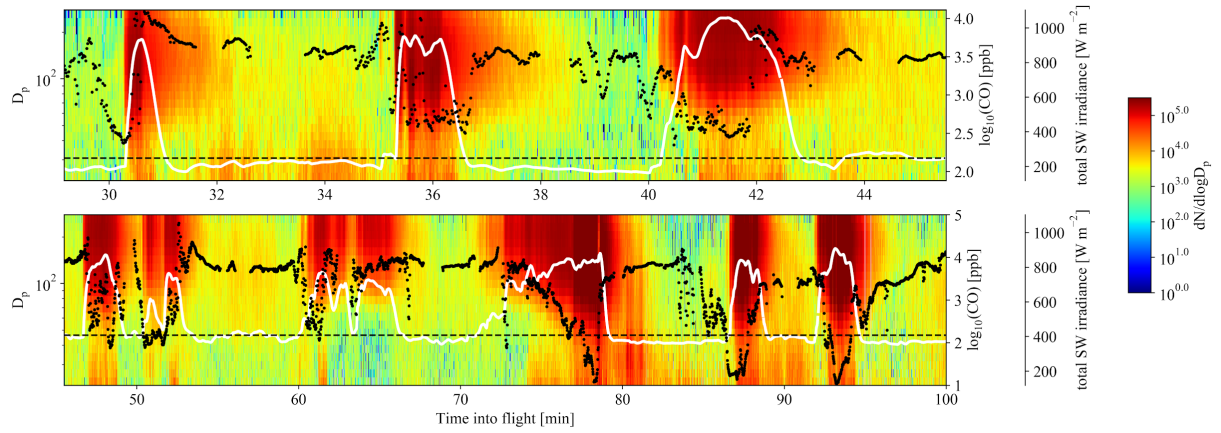


Figure S11. Number size distribution data,  $dN/d\log D_p$ , from the FIMS; CO (white solid line); and total short wave (SW) irradiance (black dots) data for the ‘821b’ flight. The bottom panel is a continuation in time from the top panel. The dotted dashed line indicates CO=150 ppb, our cutoff for in-plume/out-of-plume.

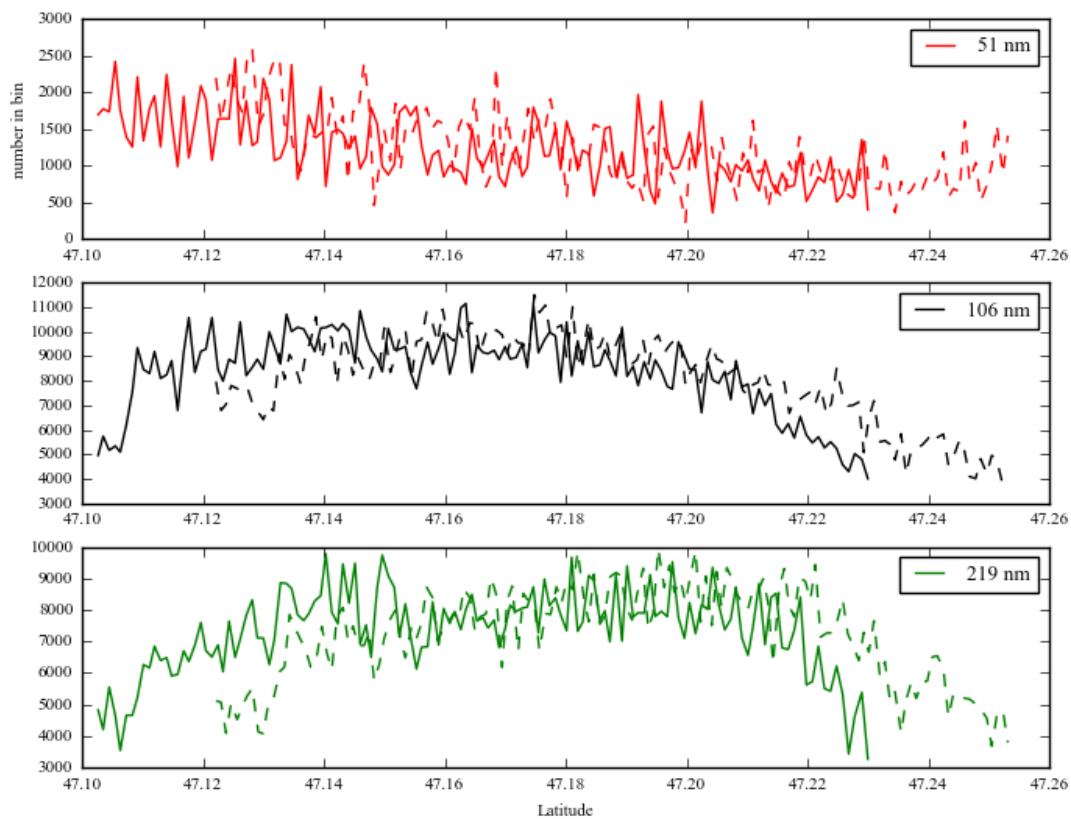


Figure S12. FIMS data for ‘809a’ for the two legs that ~overlap (Figure S5) for the 51, 106, and 219 nm size bins. The solid line is from the plane flying north to south (right to left in this figure) and the dashed line is from the plane flying south to north (left to right in this figure). In the absence of FIMS measurement artifacts, we expect these two lines to roughly match each other. Each y axis is in units of number in bin.

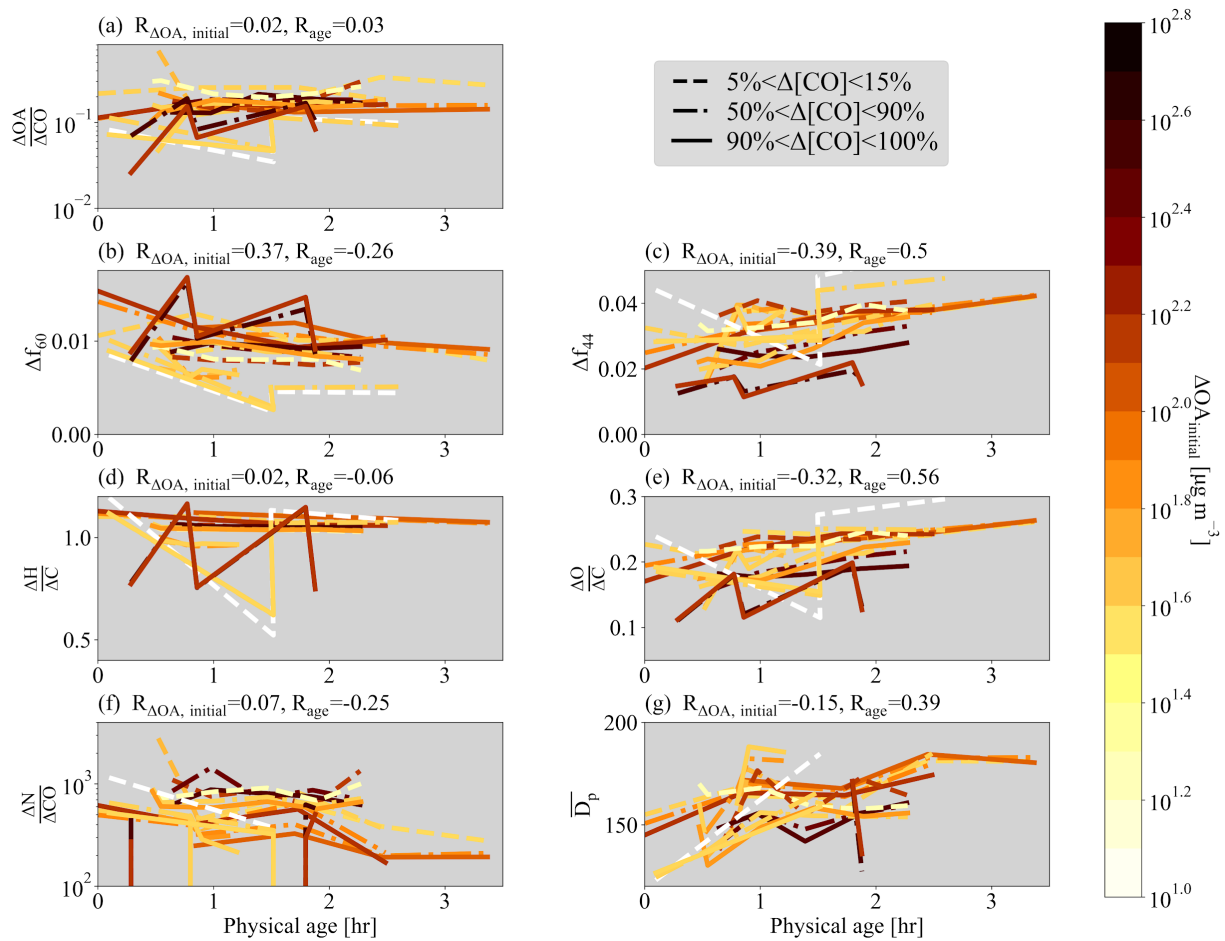


Figure S13. Same as Figure 2 but using only the first 50% of data for each leg of the FIMS and CO data for panels f-g.

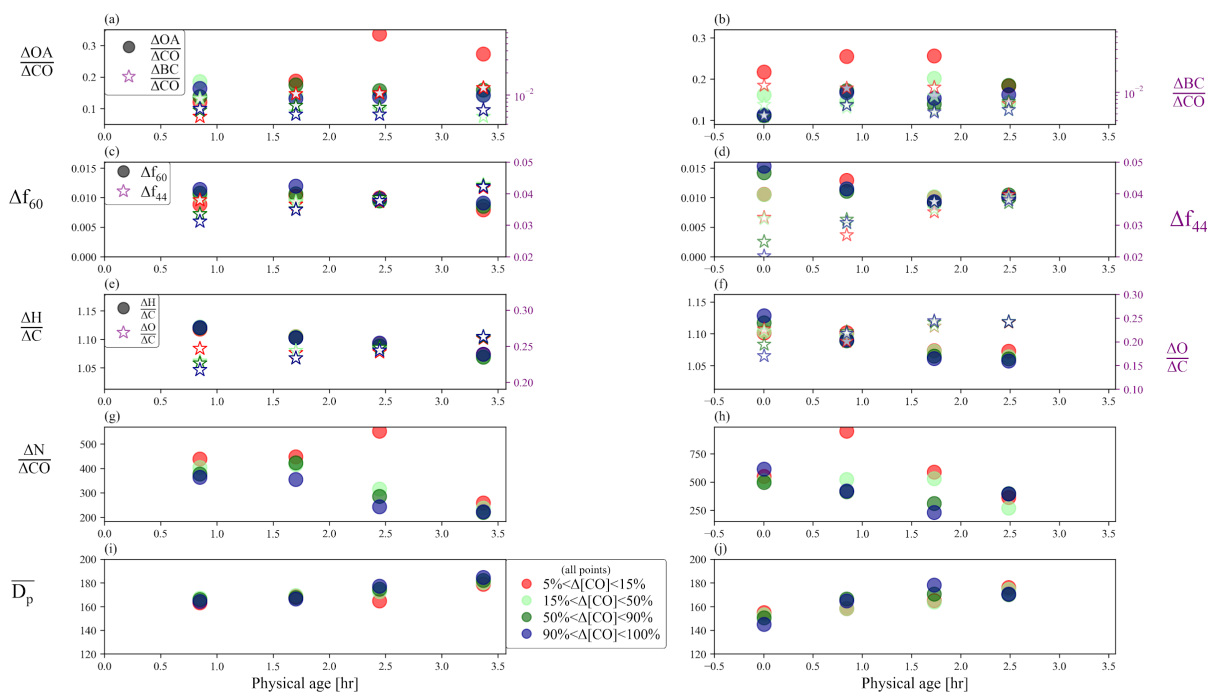


Figure S14. Aerosol properties for the first set (left-hand column) and second set (right-hand column) of pseudo-Lagrangian transects from flight ‘726a’ (a-b)  $\Delta\text{OA}/\Delta\text{CO}$  (right y-axis) and  $\Delta\text{BC}/\Delta\text{CO}$  (left y-axis), (c-d)  $\Delta f_{60}$  (right y-axis) and  $\Delta f_{44}$  (left y-axis), (e-f)  $\Delta\text{H}/\Delta\text{C}$  (right y-axis) and  $\Delta\text{O}/\Delta\text{C}$  (left y-axis), (g-h)  $\Delta\text{N}/\Delta\text{CO}$ , and (i-j)  $\overline{D}_p$  against physical age. For each transect, the data is divided into edge (the lowest 5-15% of  $\Delta\text{CO}$  data; red points), core (90-100% of  $\Delta\text{CO}$  data; blue points), and intermediate regions (15-50% and 50-90% of  $\Delta\text{CO}$  data; light green and dark green points).  $\Delta\text{BC}/\Delta\text{CO}$  is shown in log scale and the x-axis for the right-hand column has been shifted backwards to improve clarity. Note that the left-hand and right-hand columns do not always have the same y-axis limits.

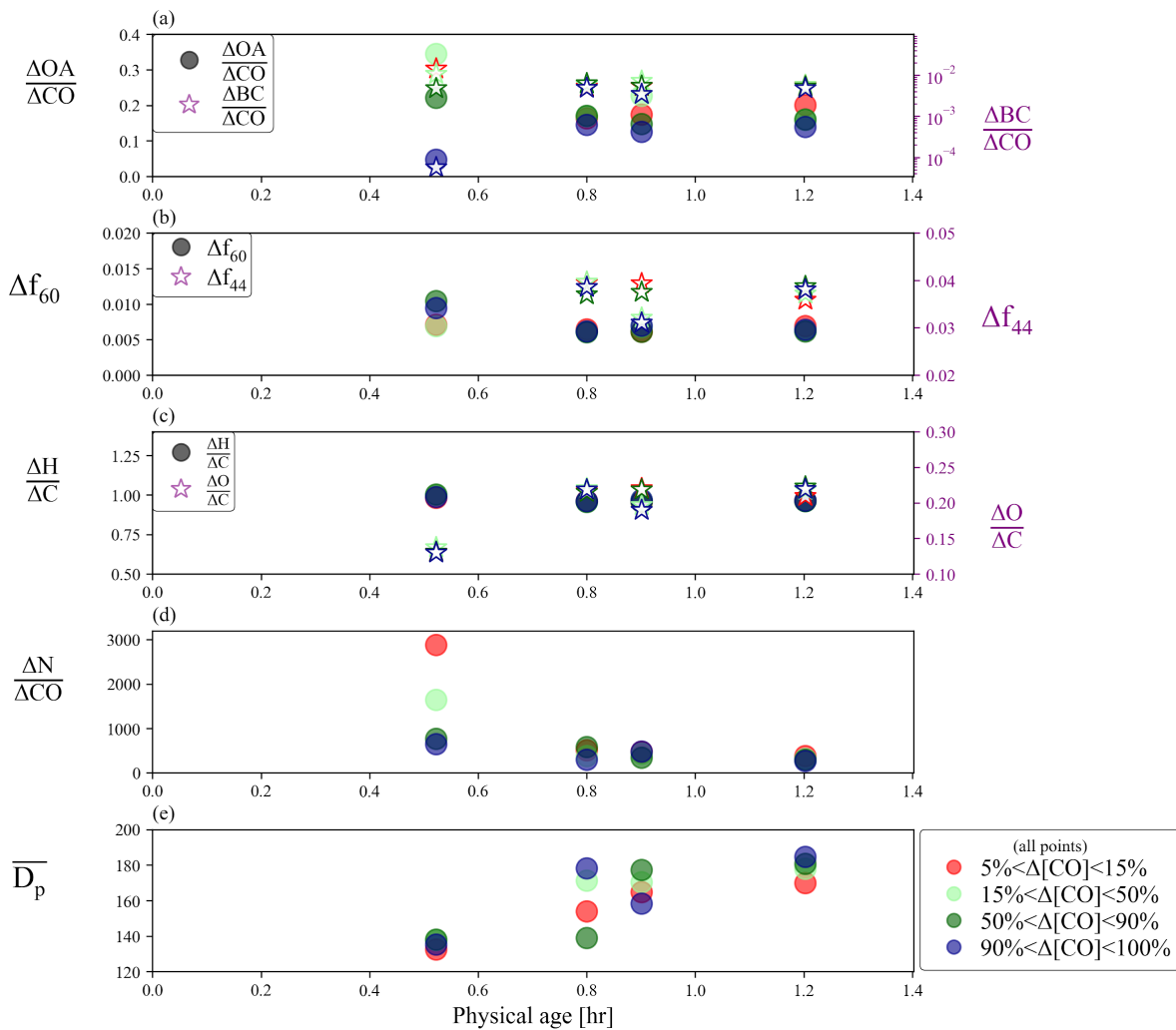


Figure S15. Aerosol properties for the set of pseudo-Lagrangian transects from flight ‘730a’ (a)  $\Delta\text{OA}/\Delta\text{CO}$  (right y-axis) and  $\Delta\text{BC}/\Delta\text{CO}$  (left y-axis), (b)  $\Delta f_{60}$  (right y-axis) and  $\Delta f_{44}$  (left y-axis), (c)  $\Delta\text{H}/\Delta\text{C}$  (right y-axis) and  $\Delta\text{O}/\Delta\text{C}$  (left y-axis), (d)  $\Delta\text{N}/\Delta\text{CO}$ , and (e)  $\overline{D}_p$  against physical age. For each transect, the data is divided into edge (the lowest 5-15% of  $\Delta\text{CO}$  data; red points), core (90-100% of  $\Delta\text{CO}$  data; blue points), and intermediate regions (15-50% and 50-90% of  $\Delta\text{CO}$  data; light green and dark green points).  $\Delta\text{BC}/\Delta\text{CO}$  is shown in log scale to improve clarity.

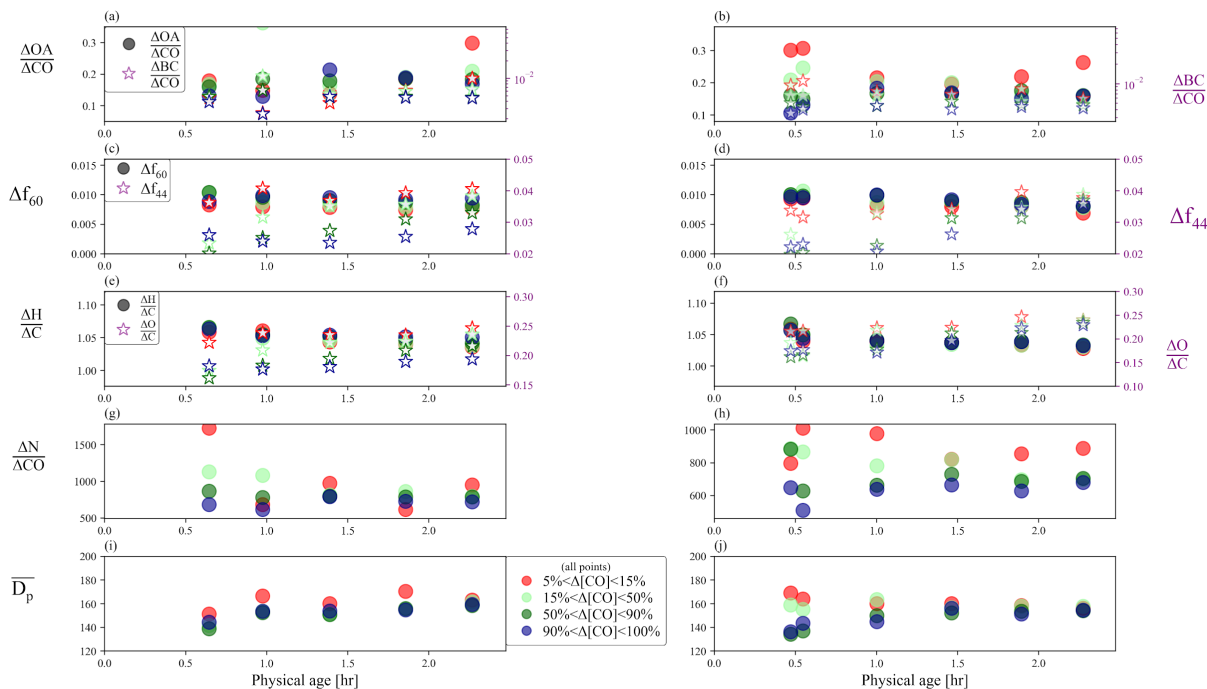


Figure S16. Aerosol properties for the first set (left-hand column) and second set (right-hand column) of pseudo-Lagrangian transects from flight ‘730b’ (a-b)  $\Delta\text{OA}/\Delta\text{CO}$  (right y-axis) and  $\Delta\text{BC}/\Delta\text{CO}$  (left y-axis), (c-d)  $\Delta f_{60}$  (right y-axis) and  $\Delta f_{44}$  (left y-axis), (e-f)  $\Delta\text{H}/\Delta\text{C}$  (right y-axis) and  $\Delta\text{O}/\Delta\text{C}$  (left y-axis), (g-h)  $\Delta\text{N}/\Delta\text{CO}$ , and (i-j)  $\overline{D}_p$  against physical age. For each transect, the data is divided into edge (the lowest 5-15% of  $\Delta\text{CO}$  data; red points), core (90-100% of  $\Delta\text{CO}$  data; blue points), and intermediate regions (15-50% and 50-90% of  $\Delta\text{CO}$  data; light green and dark green points).  $\Delta\text{BC}/\Delta\text{CO}$  is shown in log scale to improve clarity. Note that the left-hand and right-hand columns do not always have the same y-axis limits.

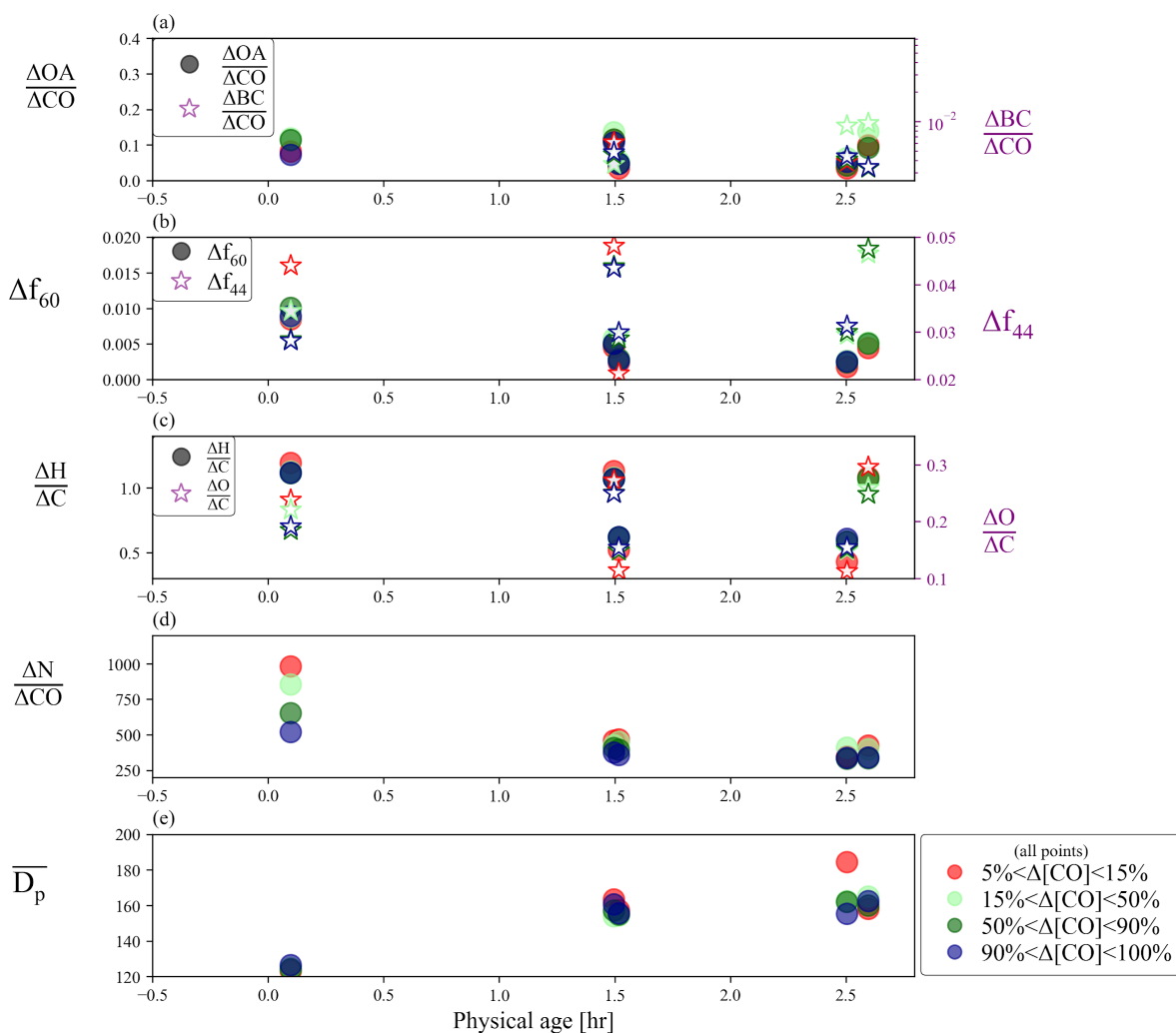


Figure S17. Aerosol properties for the set of pseudo-Lagrangian transects from flight ‘809a’ (a)  $\Delta\text{OA}/\Delta\text{CO}$  (right y-axis) and  $\Delta\text{BC}/\Delta\text{CO}$  (left y-axis), (b)  $\Delta f_{60}$  (right y-axis) and  $\Delta f_{44}$  (left y-axis), (c)  $\Delta\text{H}/\Delta\text{C}$  (right y-axis) and  $\Delta\text{O}/\Delta\text{C}$  (left y-axis), (d)  $\Delta\text{N}/\Delta\text{CO}$ , and (e)  $\overline{D}_p$  against physical age.

For each transect, the data is divided into edge (the lowest 5-15% of  $\Delta\text{CO}$  data; red points), core (90-100% of  $\Delta\text{CO}$  data; blue points), and intermediate regions (15-50% and 50-90% of  $\Delta\text{CO}$  data; light green and dark green points).  $\Delta\text{BC}/\Delta\text{CO}$  is shown in log scale and the x-axis for the right-hand column has been shifted backwards to improve clarity.

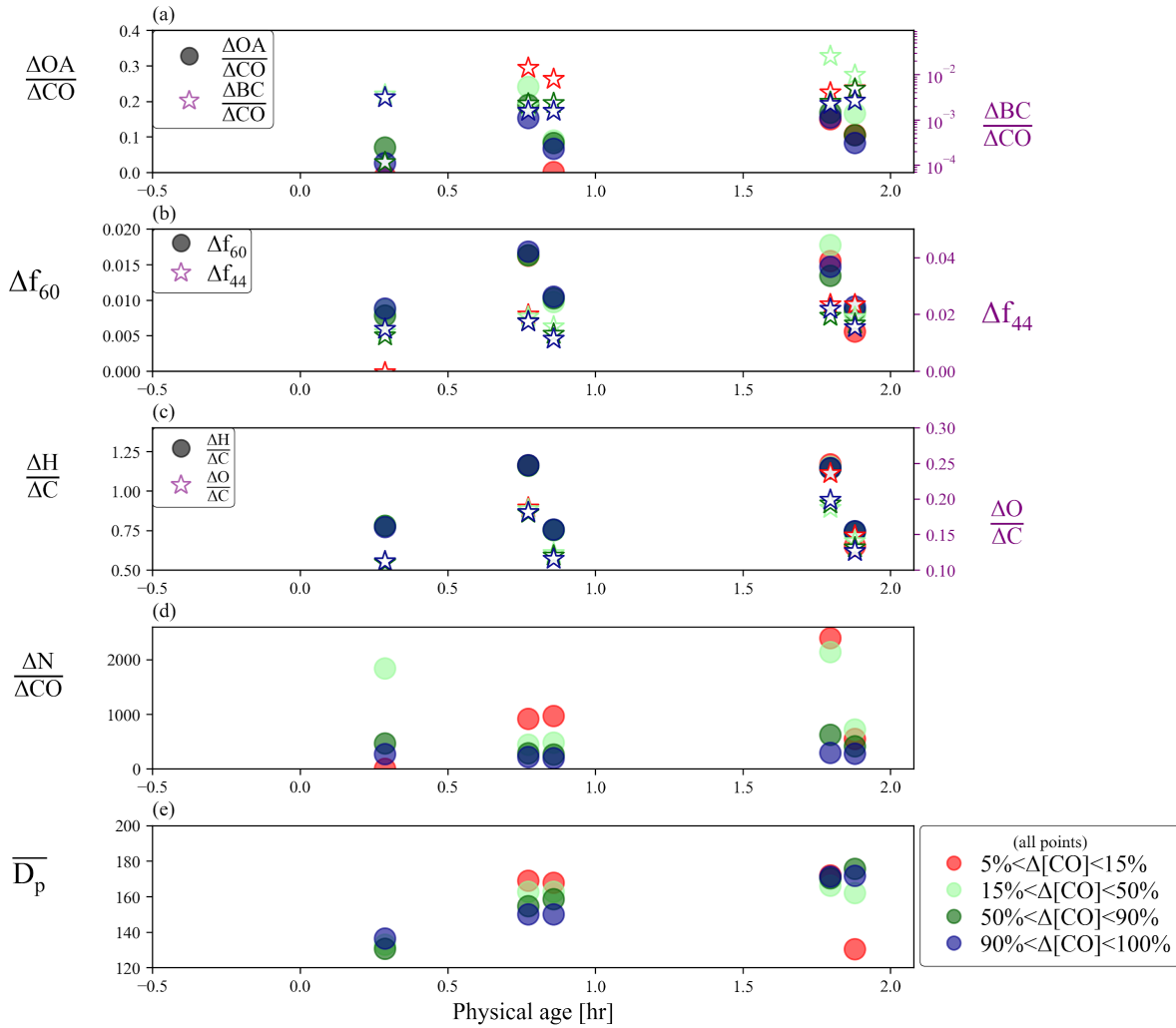


Figure S18. Aerosol properties for the set of pseudo-Lagrangian transects from flight ‘821b’ (a)  $\Delta\text{OA}/\Delta\text{CO}$  (right y-axis) and  $\Delta\text{BC}/\Delta\text{CO}$  (left y-axis), (b)  $\Delta f_{60}$  (right y-axis) and  $\Delta f_{44}$  (left y-axis), (c)  $\Delta\text{H}/\Delta\text{C}$  (right y-axis) and  $\Delta\text{O}/\Delta\text{C}$  (left y-axis), (d)  $\Delta\text{N}/\Delta\text{CO}$ , and (e)  $\overline{D}_p$  against physical age. For each transect, the data is divided into edge (the lowest 5-15% of  $\Delta\text{CO}$  data; red points), core (90-100% of  $\Delta\text{CO}$  data; blue points), and intermediate regions (15-50% and 50-90% of  $\Delta\text{CO}$  data; light green and dark green points).  $\Delta\text{BC}/\Delta\text{CO}$  is shown in log scale and the x-axis for the right-hand column has been shifted backwards to improve clarity.

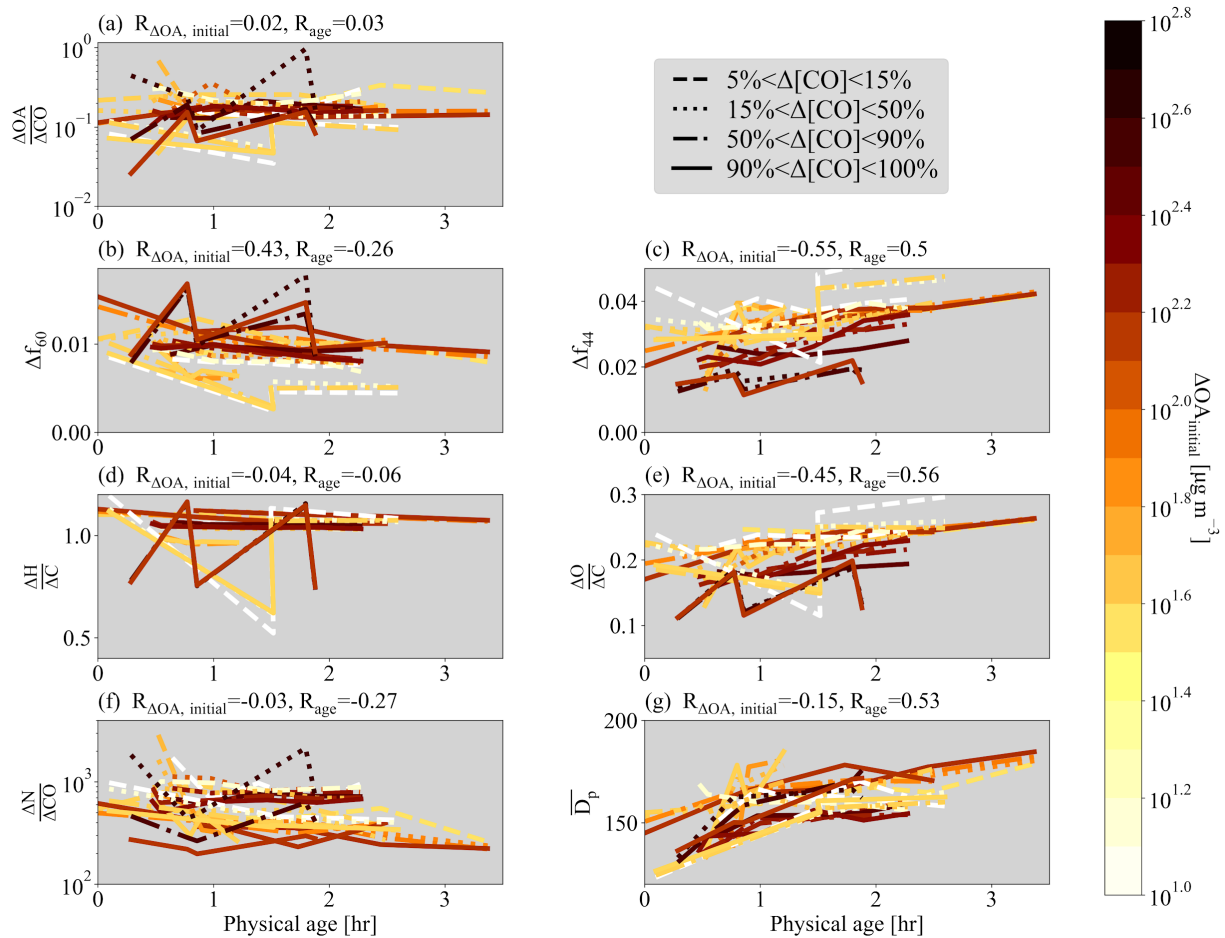


Figure S19. Various normalized parameters as a function of age for the 7 sets of pseudo-Lagrangian transects. Separate lines are shown for the edges (lowest 5-15% of  $\Delta CO$ ; dashed lines) cores (highest 90-100% of  $\Delta CO$ ; solid lines), and intermediate regions (15-50% and 50-90%; dotted and dashed-dot lines). (a)  $\Delta OA/\Delta CO$ , (b)  $\Delta f_{60}$ , (c)  $\Delta f_{44}$ , (d)  $\Delta H/\Delta C$ , (e)  $\Delta O/\Delta C$ , (f)  $\Delta N_{40-262 \text{ nm}}/\Delta CO$ , and (g)  $\overline{D}_p$  between 40-262 nm against physical age for all flights, colored by  $\Delta OA_{initial}$ . Some flights have missing data. Also provided is the Spearman correlation coefficient,  $R$ , between each variable and  $\Delta OA_{initial}$  and physical age for each variable. Note that panels (a) and (f) have a log y-axis.

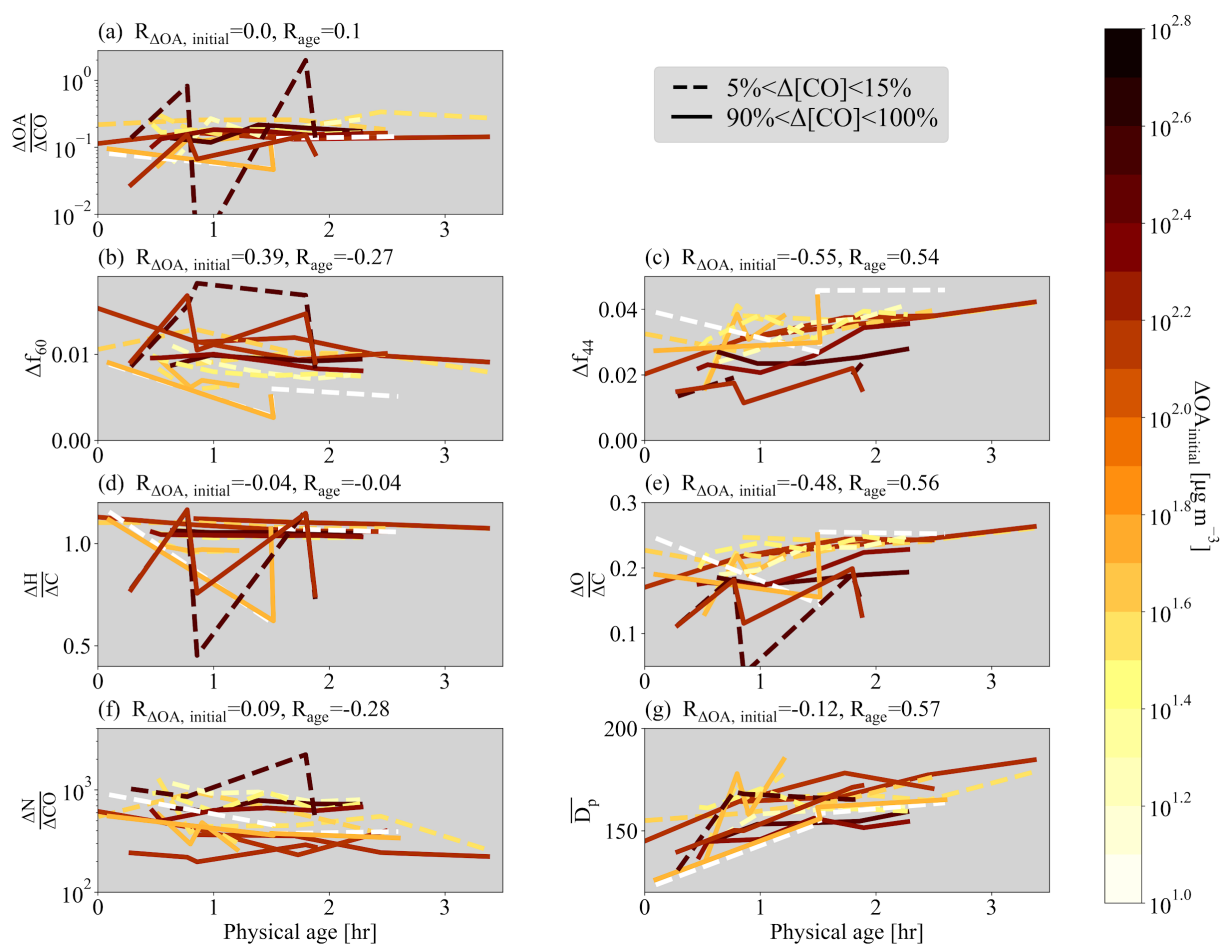


Figure S20. Various normalized parameters as a function of age for the 7 sets of pseudo-Lagrangian transects. Separate lines are shown for the edges (lowest 5-15% of  $\Delta CO$ ; dashed lines) and cores (highest 90-100% of  $\Delta CO$ ; solid lines). (a)  $\Delta OA/\Delta CO$ , (b)  $\Delta f_{60}$ , (c)  $\Delta f_{44}$ , (d)  $\Delta H/\Delta C$ , (e)  $\Delta O/\Delta C$ , (f)  $\Delta N_{40-262\text{ nm}}/\Delta CO$ , and (g)  $\overline{D}_p$  between 40-262 nm against physical age for all flights, colored by  $\Delta OA_{initial}$ . Some flights have missing data. Also provided is the Spearman correlation coefficient,  $R$ , between each variable and  $\Delta OA_{initial}$  and physical age for each variable. Note that panels (a) and (f) have a log y-axis. This figure is identical to Figure 2 but uses an in-plume CO cutoff of 200 ppb.

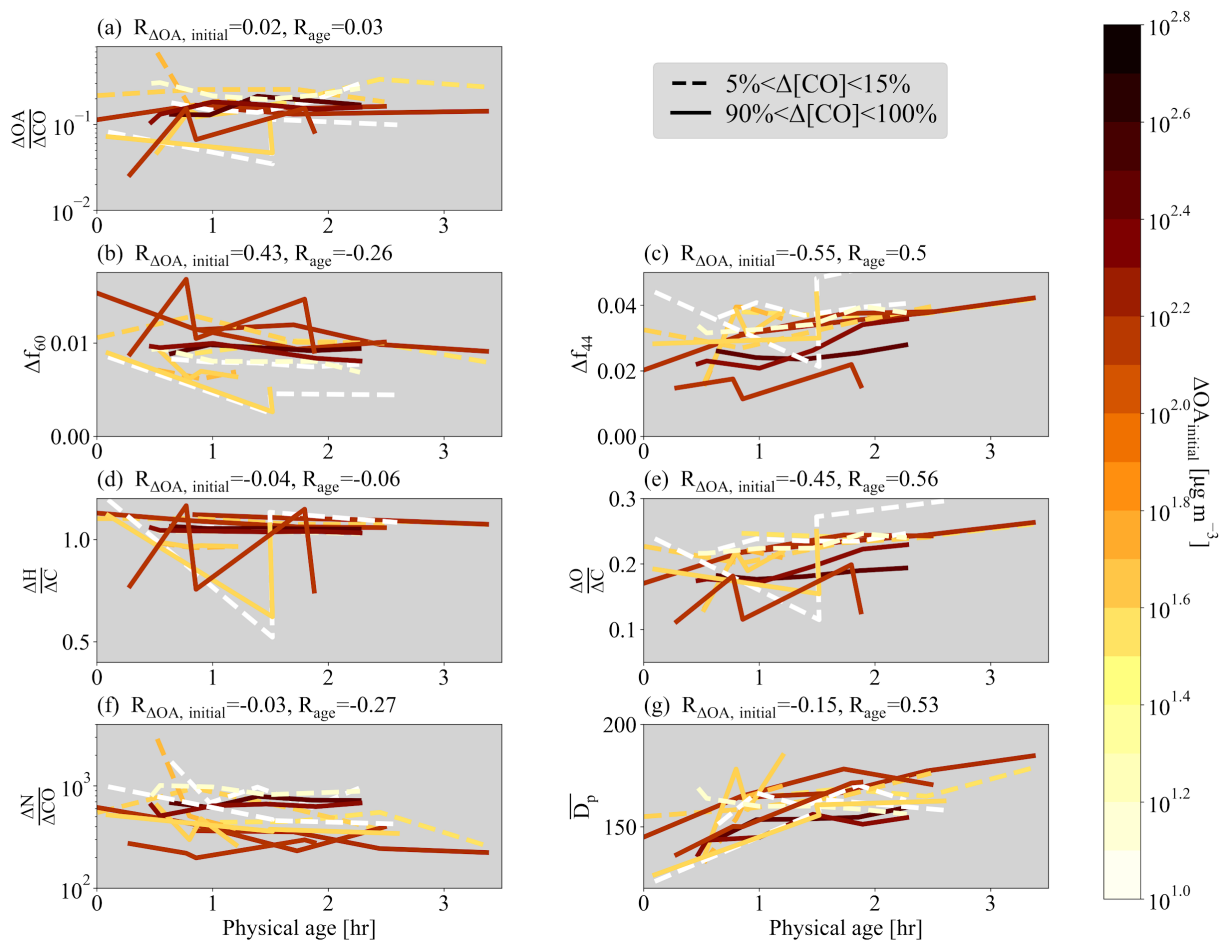


Figure S21. Various normalized parameters as a function of age for the 7 sets of pseudo-Lagrangian transects. Separate lines are shown for the edges (lowest 5-25% of  $\Delta CO$ ; dashed lines) and cores (highest 75-100% of  $\Delta CO$ ; solid lines). (a)  $\Delta OA/\Delta CO$ , (b)  $\Delta f_{60}$ , (c)  $\Delta f_{44}$ , (d)  $\Delta H/\Delta C$ , (e)  $\Delta O/\Delta C$ , (f)  $\Delta N_{40-262 \text{ nm}}/\Delta CO$ , and (g)  $\overline{D}_p$  between 40-262 nm against physical age for all flights, colored by  $\Delta OA_{\text{initial}}$ . Some flights have missing data. Also provided is the Spearman correlation coefficient,  $R$ , between each variable and  $\Delta OA_{\text{initial}}$  and physical age for each variable. Note that panels (a) and (f) have a log y-axis. This figure is identical to Figure 2 but uses different  $\Delta CO$  percentile widths.

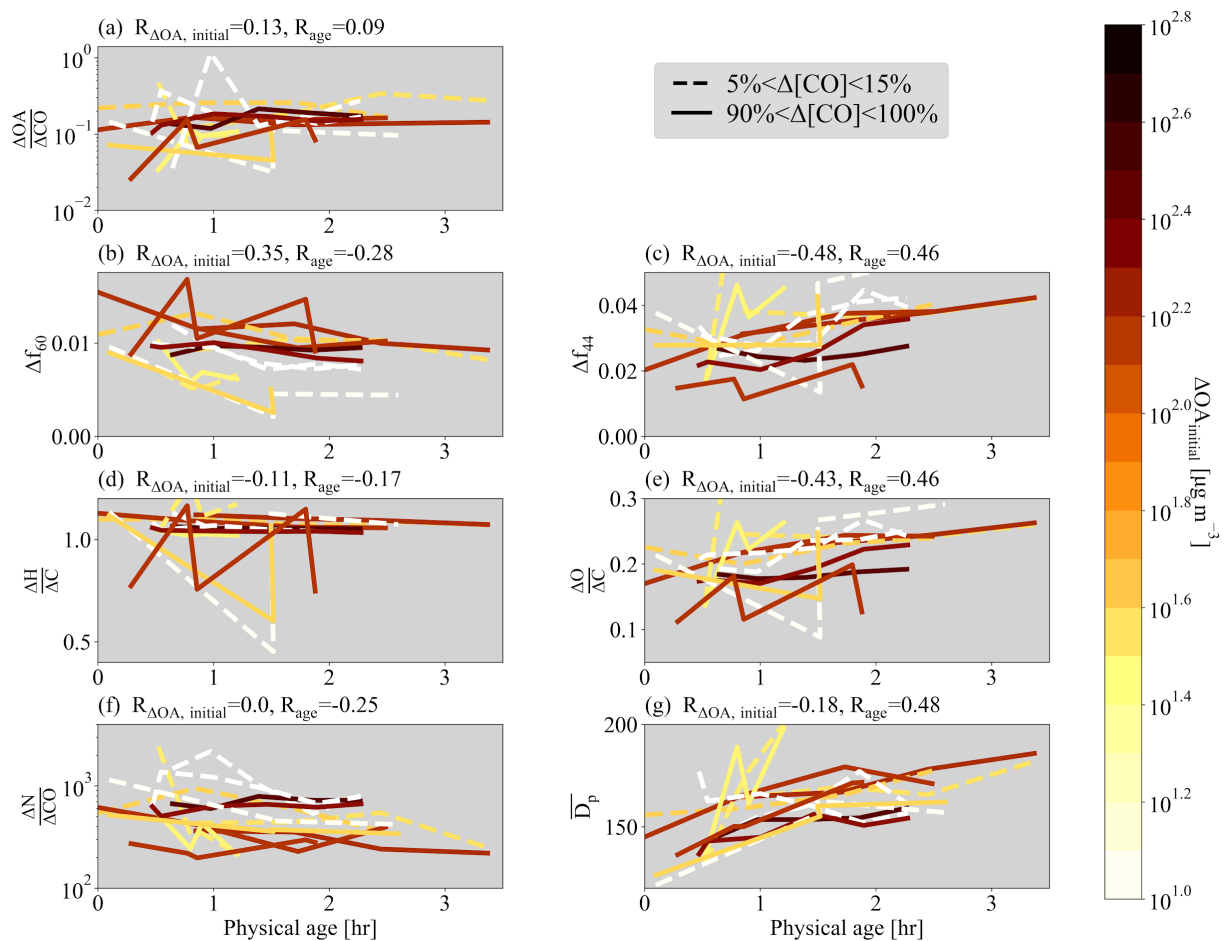


Figure S22. Various normalized parameters as a function of age for the 7 sets of pseudo-Lagrangian transects. Separate lines are shown for the edges (lowest 5-15% of  $\Delta CO$ ; dashed lines) and cores (highest 90-100% of  $\Delta CO$ ; solid lines). (a)  $\Delta OA/\Delta CO$ , (b)  $\Delta f_{60}$ , (c)  $\Delta f_{44}$ , (d)  $\Delta H/\Delta C$ , (e)  $\Delta O/\Delta C$ , (f)  $\Delta N_{40-262\text{ nm}}/\Delta CO$ , and (g)  $\overline{D}_p$  between 40-262 nm against physical age for all flights, colored by  $\Delta OA_{initial}$ . Some flights have missing data. Also provided is the Spearman correlation coefficient,  $R$ , between each variable and  $\Delta OA_{initial}$  and physical age for each variable. Note that panels (a) and (f) have a log y-axis. This figure is identical to Figure 2 except that it uses the location of the lowest 25% of CO data to determine the background concentrations of each species.

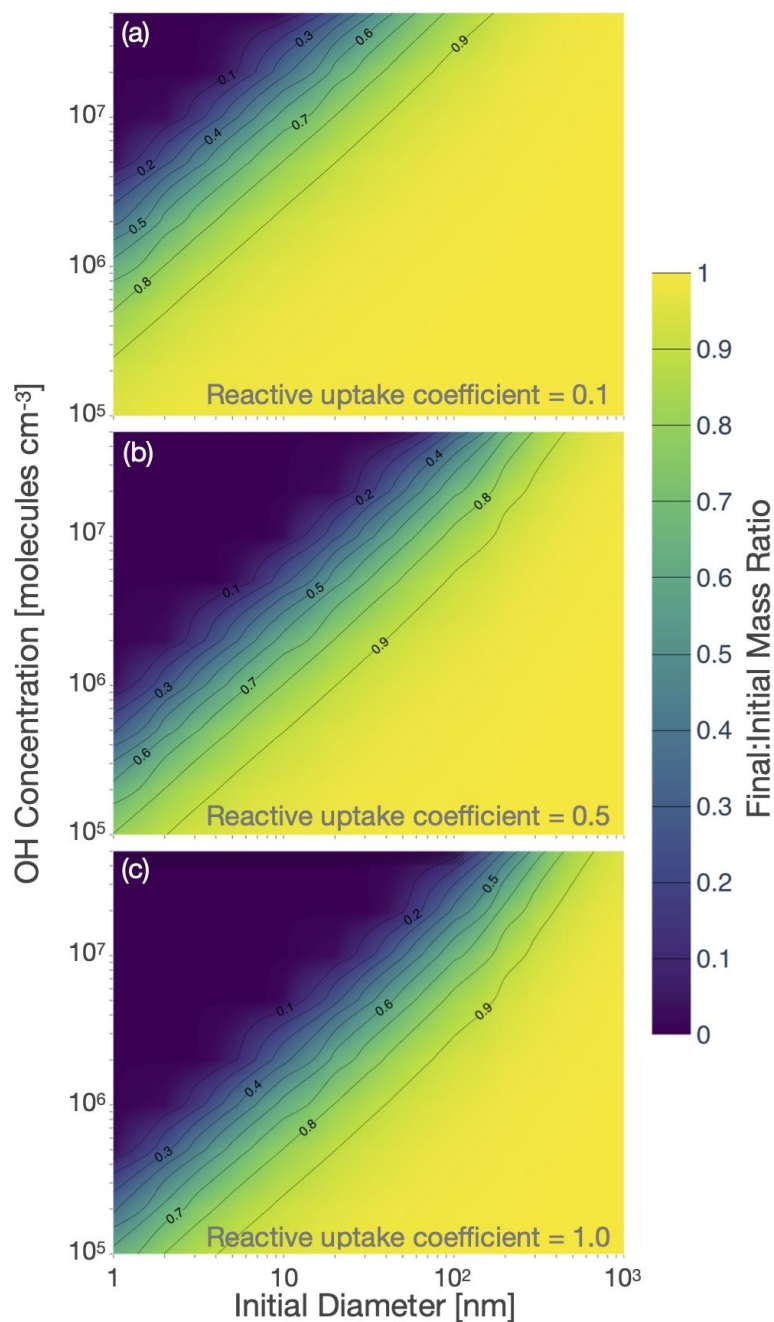


Figure S23. Calculated (final aerosol mass):(initial aerosol mass) ratios for mass loss through heterogeneous chemistry over a range of aerosol diameters and OH concentrations over 3 hours. As an upper-bound case, (a) it is assumed that for each OH collision, 200 amu of mass is lost. As a middle-bound, (b) it is assumed that 50% of OH collisions result in a 200 amu mass loss. As a more-realistic loss rate, (c) assumes that 10% of all OH collisions result in an 200 amu mass loss. See SI text S2 for more details.

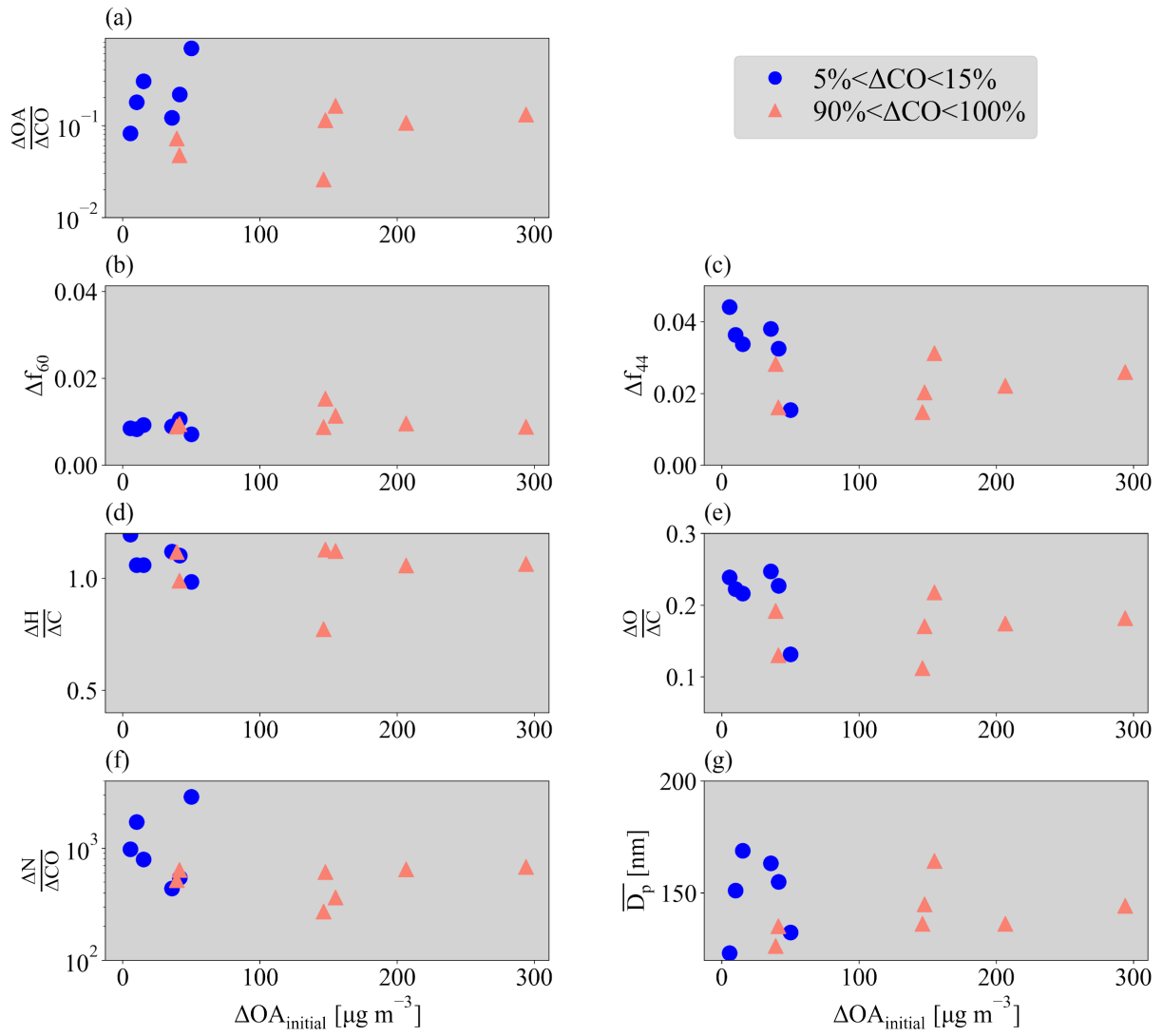


Figure S24. Scatter plot of each parameter of Figure 1 against  $\Delta OA_{\text{initial}}$ .

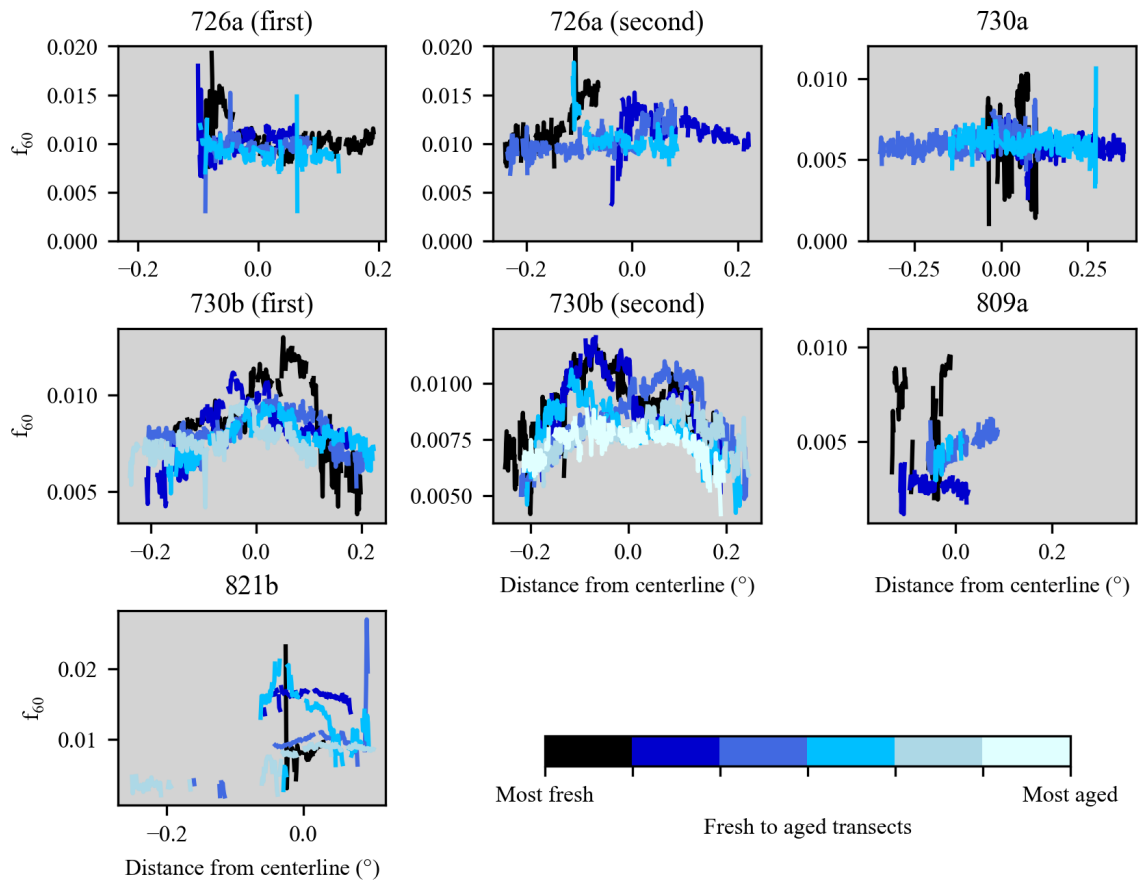


Figure S25. Raw  $f_{60}$  data for each flight along each transect included in this study. The titles indicate the flight. The black color indicates the earliest transect, with increasingly lighter colors indicating increasingly downwind transects. The centerline was estimated from the number size distribution and the estimated center of the fire (Figures S1-S6).

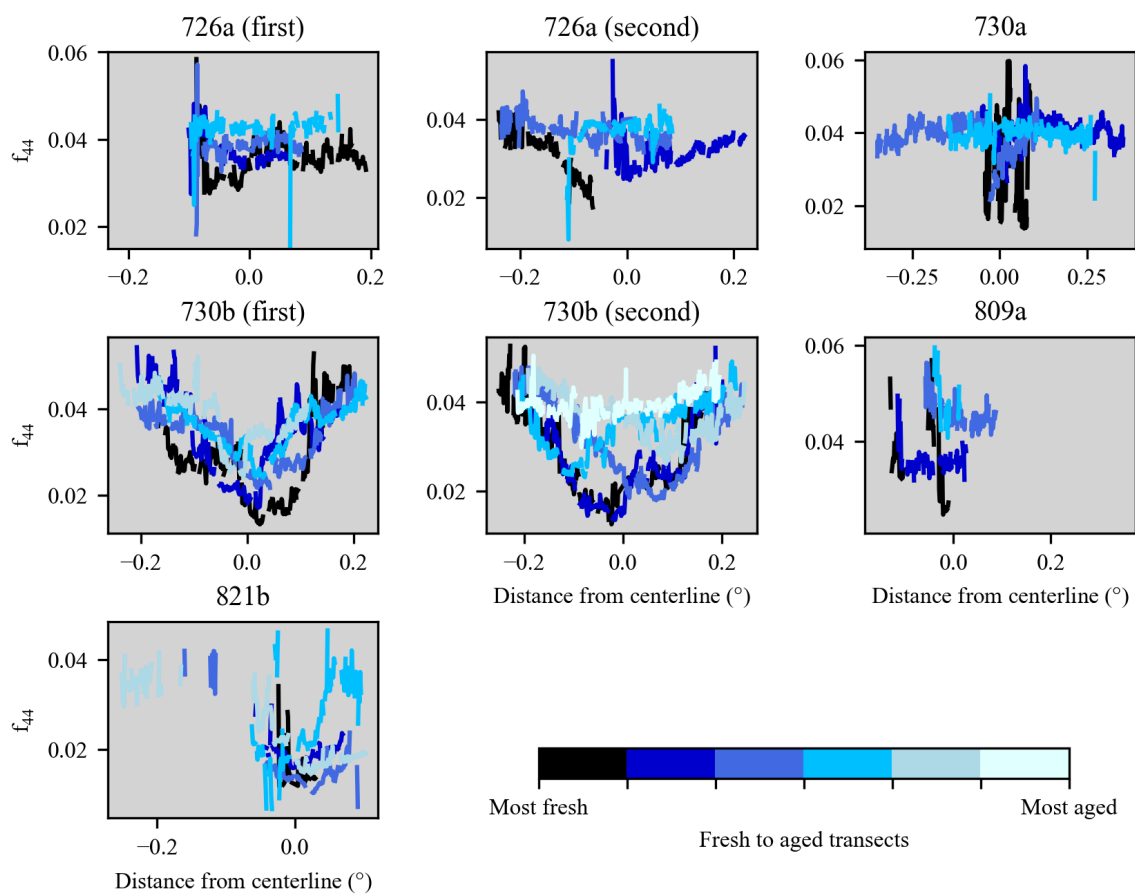


Figure S26. Raw  $f_{44}$  data for each flight along each transect included in this study. The titles indicate the flight. The black color indicates the earliest transect, with increasingly lighter colors indicating increasingly downwind transects. The centerline was estimated from the number size distribution and the estimated center of the fire (Figures S1-S6).

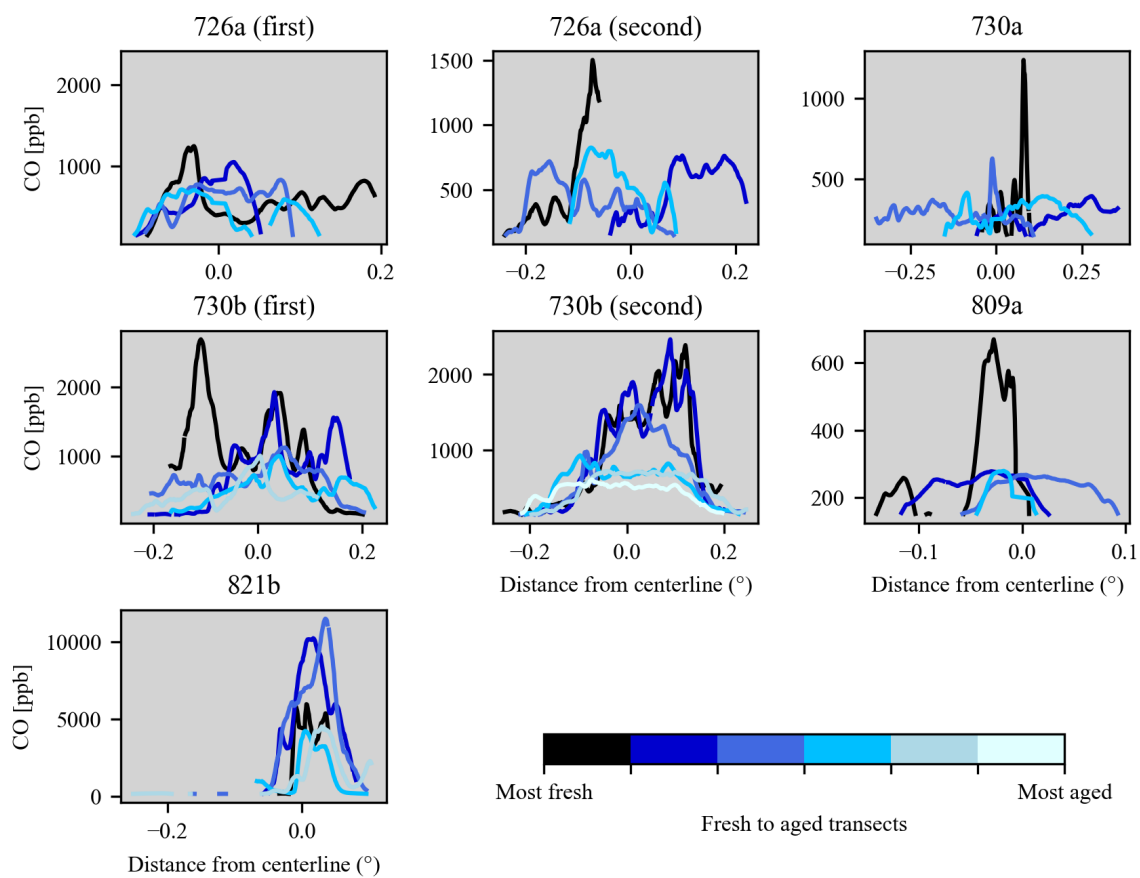


Figure S27. Total in-plume CO (ppbv) irradiance for each flight along each transect included in this study. The titles indicate the flight. The black color indicates the earliest transect, with increasingly lighter colors indicating increasingly downwind transects. The centerline was estimated from the number size distribution and the estimated center of the fire (Figures S1-S6).

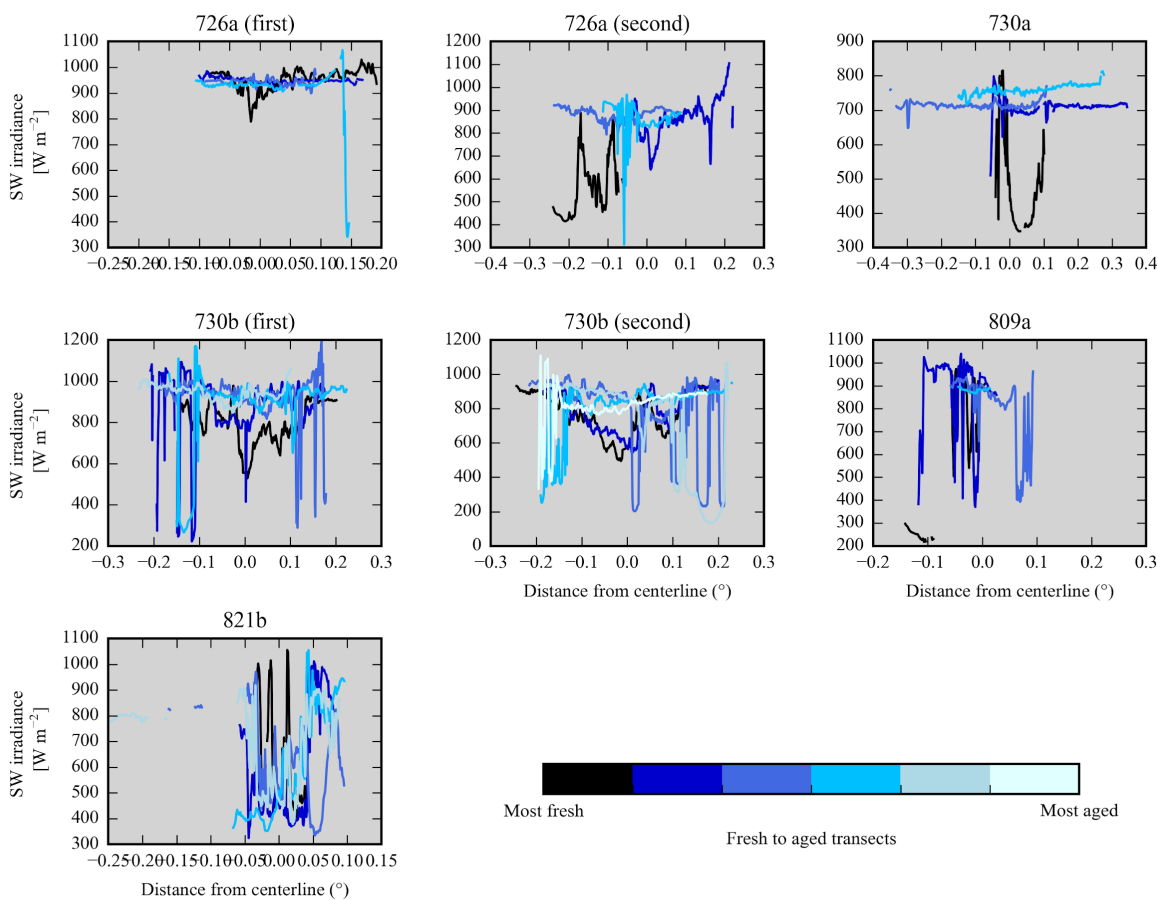


Figure S28. Total in-plume shortwave (SW) irradiance for each flight along each transect included in this study. The titles indicate the flight. The black color indicates the earliest transect, with increasingly lighter colors indicating increasingly downwind transects. The centerline was estimated from the number size distribution and the estimated center of the fire (Figures S1-S6).

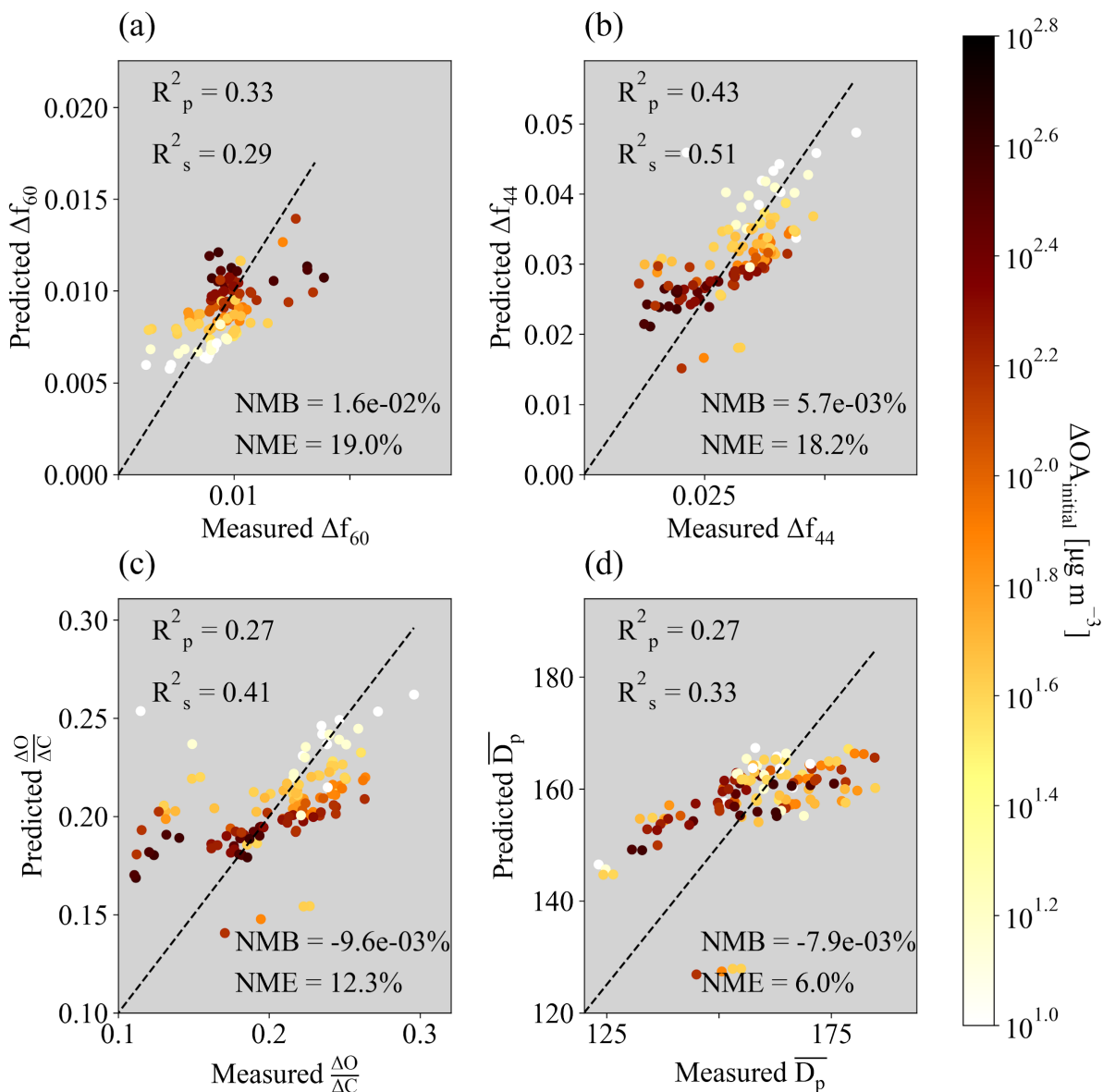


Figure S29. Measured versus predicted (a)  $\Delta f_{60}$ , (b)  $\Delta f_{44}$ , and (c)  $\overline{D}_p$  between 40-262 nm, using the equation  $\ln(X) = a \ln(\Delta OA_{initial}) + b \ln(\text{Physical age}) + c$  (Eq. 5) where  $X = \Delta f_{60}$ ,  $\Delta f_{44}$ , or  $\overline{D}_p$ . The values of a, b, and c are provided in Table S4. The Pearson and Spearman coefficients of determination ( $R_p^2$  and  $R_s^2$ , respectively) are provided in each panel, along with the normalized mean bias (NMB) and normalized mean error (NME). Included in the fit and figure are all four regions within the plume (the 5-15%, 15-50%, 50-90%, and 90-100% of  $\Delta CO$ ), all colored by the mean  $\Delta OA_{initial}$  of each  $\Delta CO$  percentile range.

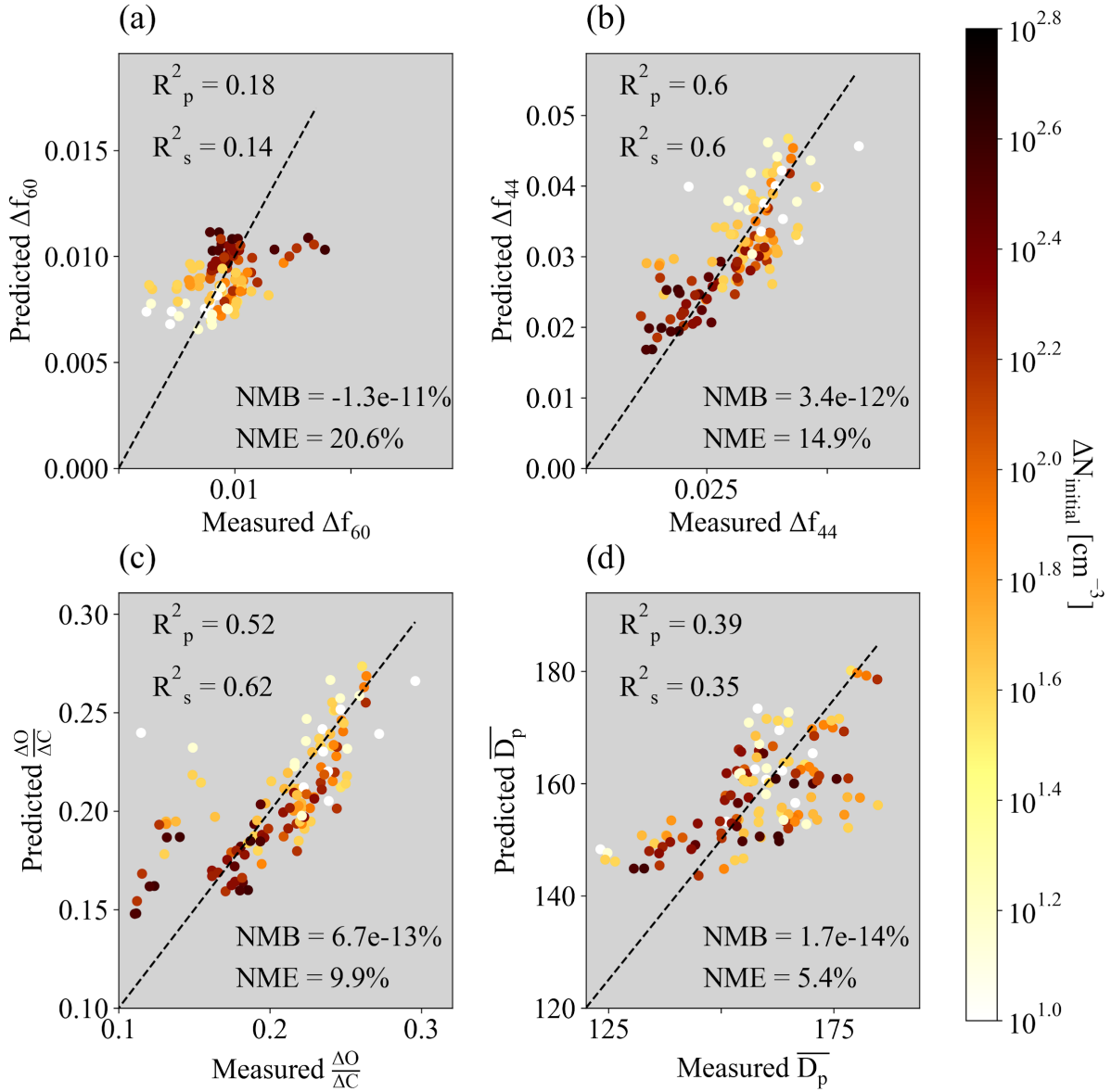


Figure S30. Measured versus predicted (a)  $\Delta f_{60}$ , (b)  $\Delta f_{44}$ , and (c)  $\overline{D}_p$  between 40-300 nm, using the equation  $X = a \log_{10}(\Delta N_{initial}) + b(\text{Physical age}) + c$  where  $X = \Delta f_{60}$ ,  $\Delta f_{44}$ , or  $\overline{D}_p$  where  $X = \Delta f_{60}$ ,  $\Delta f_{44}$ , or  $\overline{D}_p$ . Note that the fit here is the same as that in Eq. 2 except that  $\Delta N_{initial}$  replaces  $\Delta O A_{initial}$ . The values of  $a$ ,  $b$ , and  $c$  are provided in Table S5. The Pearson and Spearman coefficients of determination ( $R_p^2$  and  $R_s^2$ , respectively) are provided in each panel, along with the normalized mean bias (NMB) and normalized mean error (NME). Included in the fit and

figure are all four regions within the plume (the 5-15%, 15-50%, 50-90%, and 90-100% of  $\Delta\text{CO}$ ), all colored by the mean  $\Delta\text{OA}_{\text{initial}}$  of each  $\Delta\text{CO}$  percentile range.

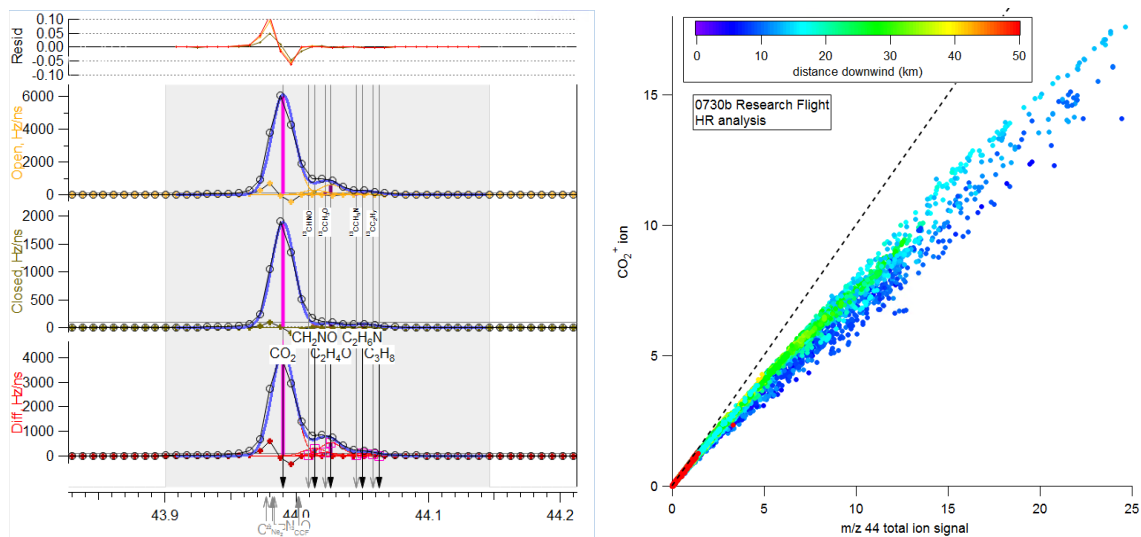


Figure S31. (a) High resolution fits at  $m/z$  44 for a biomass burning plume during 0730b research flight with laser ON. (b) Correlation of HR  $\text{CO}_2^+$  ion and HR total ion signal at  $m/z$  44, colored by distance downwind (km) from fire.



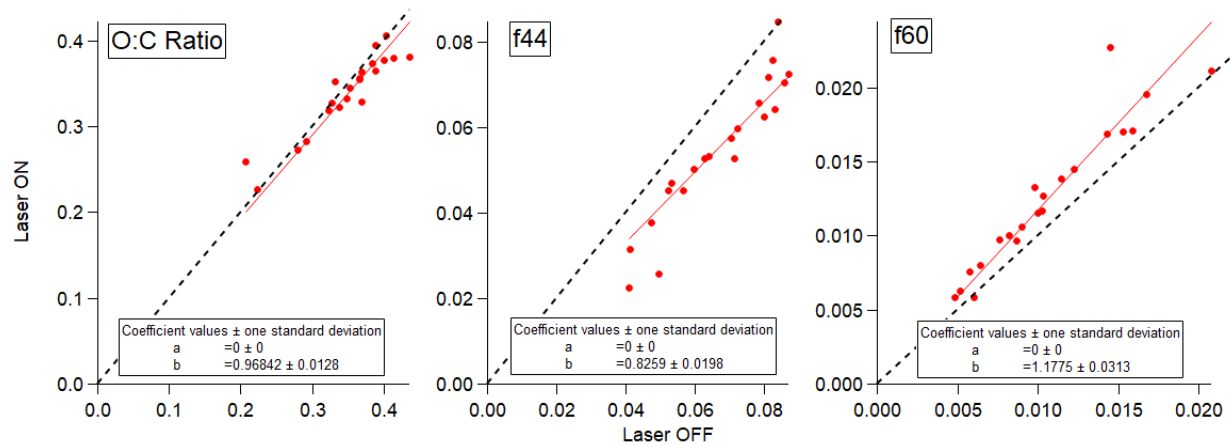


Figure S33. Laser ON versus laser OFF SP-AMS HR O:C, UMR f44, and UMR f60 ratios.